

# Predictive simulation of non-steady-state transport of gases through rubbery polymer membranes

Marielle Soniat <sup>a, b</sup>, Meron Tesfaye <sup>c, d</sup>, Daniel Brooks <sup>e</sup>, Boris Merinov <sup>e</sup>, William A. Goddard III <sup>e</sup>, Adam Z. Weber <sup>a, c</sup>, Frances A. Houle <sup>a, b, \*</sup>

<sup>a</sup> Joint Center for Artificial Photosynthesis, Lawrence Berkeley National Laboratory, Berkeley, CA 94720, USA

<sup>b</sup> Chemical Sciences Division, Lawrence Berkeley National Laboratory, Berkeley, CA 94720, USA

<sup>c</sup> Energy Storage and Distributed Resources Division, Lawrence Berkeley National Laboratory, Berkeley, CA 94720, USA

<sup>d</sup> Department of Chemical and Biomolecular Engineering, University of California, Berkeley, CA 94720, USA

<sup>e</sup> Materials and Process Simulation Center (MSC), Beckman Institute, California Institute of Technology, Pasadena, CA 91125, USA

## ARTICLE INFO

### Article history:

Received 22 August 2017

Received in revised form

14 October 2017

Accepted 22 November 2017

Available online 24 November 2017

### Keywords:

Rubbery polymers

Reaction-diffusion modeling

Gas transport

## ABSTRACT

A multiscale, physically-based, reaction-diffusion kinetics model is developed for non-steady-state transport of simple gases through a rubbery polymer. Experimental data from the literature, new measurements of non-steady-state permeation and a molecular dynamics simulation of a gas-polymer sticking probability for a typical system are used to construct and validate the model framework. Using no adjustable parameters, the model successfully reproduces time-dependent experimental data for two distinct systems: (1) O<sub>2</sub> quenching of a phosphorescent dye embedded in poly(*n*-butyl(amino)thionylphosphazene), and (2) O<sub>2</sub>, N<sub>2</sub>, CH<sub>4</sub> and CO<sub>2</sub> transport through poly(dimethyl siloxane). The calculations show that in the pre-steady-state regime, permeation is only correctly described if the sorbed gas concentration in the polymer is dynamically determined by the rise in pressure. The framework is used to predict selectivity targets for two applications involving rubbery membranes: CO<sub>2</sub> capture from air and blocking of methane cross-over in an aged solar fuels device.

© 2017 Elsevier Ltd. All rights reserved.

## 1. Introduction

Permeant transport through a polymer membrane is driven by differences in pressure, concentration, temperature, and, if it is a polyelectrolyte, the electrical potential across it [1]. The most common model is the solution-diffusion model for steady-state, which is defined in terms of the permeability,  $P_m$ . The permeability is the product of the Henry's Law solubility,  $S$ , and diffusivity,  $D$ , i.e.  $P_m = S \times D$  [2]. Models with a high level of detail concerning the physical nature of uptake and permeation are not generally available. Such models are valuable for their predictive character and their ability to provide scientific insight. This work builds a foundation for the development and use of these more detailed models in the study of transport through polymers.

Polymeric membrane materials fall into two basic classes, highly permeable rubbers with low glass transition temperatures ( $T_g$ ) and weakly permeable glasses with high  $T_g$ . The solution-diffusion model applies to both. The physical processes that take place in the polymer bulk do not depend on whether the permeant was initially present as a component of a liquid or in the gas phase. The details of the process of uptake into the membrane, on the other hand, are likely to depend on permeant phase. The solution-diffusion model assumes that no matter what the source of the permeant, its rate of uptake at the polymer interface is much faster than diffusion through the polymer bulk [3], and therefore is not rate limiting. Molecular dynamics simulations and kinetics models using parameterized schemes have provided important insights to the detailed nature of uptake and permeation for ion-conducting, phase-separated perfluorosulfonic-acid polymers [4,5]. This level of physical detail, however, is not available for most membrane systems.

Steady-state permeation as described by the solution-diffusion model is relevant to many applications using polymeric membranes such as purification and electrolyzer systems, but not to

\* Corresponding author. Chemical Sciences Division, Lawrence Berkeley National Laboratory, Berkeley, CA 94720, USA.

E-mail address: [fahoule@lbl.gov](mailto:fahoule@lbl.gov) (F.A. Houle).

## Nomenclature: List of symbols

Symbol	Meaning	Units
$A$	area	$\text{m}^2$
$B + 1$	ratio of intensities	—
$dx$	distance in x	m
$D$	diffusivity	$\text{m}^2/\text{s}$
$h$	Planck constant	J s
$I_0$	intensity of light emission in absence of $\text{O}_2$	—*
$I_{eq}$	intensity of light emission at a constant $[\text{O}_2]$	—*
$I(t)$	time-dependent light intensity	—*
$J$	flux through membrane	$\text{mol}/(\text{m}^2 \text{ s})$
$k_B$	Boltzmann constant	J/K
$k_{ads}$	pseudo-first order rate constant for adsorption	$\text{s}^{-1}$
$k_{bub}$	zeroth order rate constant for $\text{CH}_4$ to enter gas phase	$\text{mol}/(\text{L s})$
$k_{coll}$	rate constant for collision of gases with the surface	$\text{s}^{-1}$
$k_{des}$	rate constant for desorption from a surface	$\text{s}^{-1}$
$k_{ex}$	pseudo-first order rate constant for excitation of PtOEP	$\text{s}^{-1}$
$k_{hyd}$	zeroth order rate constant for $\text{CH}_4$ to enter gas phase	$\text{mol}/(\text{L s})$
$k_{nr}$	rate constant for radiative decay of PtOEP	$\text{s}^{-1}$
$k_{prod}$	zeroth order rate constant for production of $\text{CH}_4$	$\text{mol}/(\text{L s})$
$k_q$	rate constant for quenching of PtOEP by $\text{O}_2$	$\text{L}/(\text{mol s})$
$k_r$	rate constant for emission of photons from PtOEP	$\text{s}^{-1}$
$k_{TTA}$	rate constant for TTA	$\text{L}/(\text{mol s})$
$l$	thickness of the membrane	m
$m_w$	molecular mass	kg/mol
$n$	amount of gas	mol
$n_{max}$	maximum amount of gas	mol
$N_{Av}$	Avogadro's number	molecules/mol
$P_m$	permeability of the membrane	$(\text{mol m})/(\text{m}^2 \text{ s Pa})$
		for gas phase
		$\text{m}^2/\text{s}$
		for liquid phase
$p_{ds}$	downstream pressure	Pa
$p_{O_2}$	external partial pressure of $\text{O}_2$	Pa
$p_{up}$	upstream pressure	Pa
$\Delta p$	difference between upstream and downstream pressures	Pa
$r_{sun}$	ratio of current sunlight level to maximum sunlight level	—
$R$	universal gas constant	J/(mol K)
$R_{AB}$	encounter distance	m
$S$	solubility	$\text{mol}/(\text{L Pa})$
		for gas phase
		$(\text{mol/L})/(\text{mol/L})$
		for liquid phase
$t$	time	s
$T$	temperature	K
$V$	volume	$\text{m}^3$
$V_{ds}$	downstream volume	$\text{m}^3$
$x$	position	m
$Z$	collision frequency	$\text{s}^{-1}$
$\mu$	sticking probability	—
$\nu_L$	frequency of exciting light	m
$\pi$	pi	—
$\rho$	mass density	$\text{kg}/\text{m}^3$
$\sigma_a$	absorption cross section	$\text{m}^2$
$\tau$	lifetime of $^3\text{PtOEP}$ in the presence of a constant $[\text{O}_2]$	s
$\tau_0$	lifetime of $^3\text{PtOEP}$ in the absence of $\text{O}_2$	s
$\Phi_P$	phosphorescence quantum yield	—
$\chi$	rate	$\text{mol}/(\text{L s})$
$\omega_L$	energy density	J/ $\text{m}^2$
$[\text{gas}_{(p)}]$	concentration of a gas within the polymer	mol/L
$[\text{O}_{2(p)}]_{eq}$	concentration of $\text{O}_2$ within the polymer at equilibrium	mol/L
$[\text{O}_{2(p)}](x,t)$	concentration of $\text{O}_2$ within the polymer as a function of position and time	mol/L
$[\text{PtOEP}]$	total concentration of PtOEP	mol/L
$[\text{PtOEP}]_{init}$	initial concentration of excited-state PtOEP	mol/L

\*All reported intensities are normalized and so unitless.

those in which permeant concentrations and other operating conditions such as temperature vary significantly with time. Examples are gas sensor and intermittent gas separations systems, electrolyzers using electricity from renewable sources, or photo-electrochemical systems that use sunlight to convert components of air and water into fuels. The membrane composition and structure required for each of these applications varies, and at our

current level of understanding the physical details governing time-dependent membrane performance cannot be assumed to be as simple to capture as they are by the solution-diffusion model. To begin to develop a description of membrane behaviors far from steady state, we focus in this study on one extreme – inert gases permeating a rubbery polymer. Our basic model is constructed in a manner that enables it to be extended to more complex situations

such as mixed-matrix membranes, metal foam separators, permeant-induced ageing, permeation of mixtures whose transport properties through the membrane are not independent of each other, and permeation under variable temperature conditions. The ability to model such situations predictively allows membrane architectures well-suited for time-varying applications to be developed.

The rubbery, non-interacting regime applies to membranes for gas sensors and certain gas separators. We consider time-dependent permeation in two configurations: (1) reversible permeation of gases into a gas-sensor system, and (2) pre-steady-state transport through a gas separator. Time-dependent data for a sensor system have been reported in the literature [6–8]. For the present work, we examine a comprehensive data set describing quenching of phosphorescence of a dye in a series of rubbery polymers by O<sub>2</sub> and have used them to develop and validate a basic model framework. Time-dependent gas-separator data obtained under well-controlled conditions are scarce, so we have measured non-steady-state permeation of gases over a range of pressures through a rubbery polymer, polydimethylsiloxane (PDMS) for this work. The gases - O<sub>2</sub>, N<sub>2</sub>, CO<sub>2</sub>, and CH<sub>4</sub> - are selected to span a range of gas solubilities and nature of interaction with the polymer chains. We have examined aspects of uptake by using molecular dynamics simulations to estimate the fraction of CO<sub>2</sub>-PDMS collisions that result in adsorption or absorption. Using these data, a multiscale, reaction-diffusion model framework has been constructed that successfully reproduces both sensor and separator data with no adjustable parameters, and reveals several aspects of the permeation process that are kinetically significant. Because it is predictive, the model is useful to examine functional systems. As an example, we describe simulation results for use of rubbery membranes to separate gas mixtures, and product crossover between cathode and anode chambers during a diurnal cycle of a solar-driven photoelectrochemical CO<sub>2</sub> reduction system. The latter case is applicable to a system in which the membrane has become rubbery due to prolonged exposure to CO<sub>2</sub>.

## 2. Methods and materials

Three separate methodologies have been combined in the present study: stochastic reaction-diffusion simulations, molecular-dynamics simulations, and gas-permeation measurements. The materials set considered in this work is shown in Fig. 1.

### 2.1. Reaction-diffusion simulations

The goal of this work is to develop a predictive model whose simulation outputs can be compared directly to experimental data. This requires that all simulation inputs (system geometry, rate constants and concentrations of all reactants and products) be measured.

Experimentally, calculated by molecular dynamics simulations, or derived from established theory. The simulation reaction-diffusion code used in this study incorporates stochastic methods, a type of kinetic Monte Carlo that produces an accurate timebase [9,10]. It provides a rigorously accurate solution to the master equation for Markov systems, and is a useful alternative to coupled differential equation integrators for complex materials systems. It is particularly well-suited for systems that require detail at both nanoscale and macroscale dimensions, and involve large dynamic ranges in rates. The open access code package is Kinetiscope [11]. Details on its computational methodology and applications to various types of condensed organic phase reaction-diffusion systems are described in previous publications [12–17]. The basic framework used in this work is a 1-dimensional reaction-diffusion

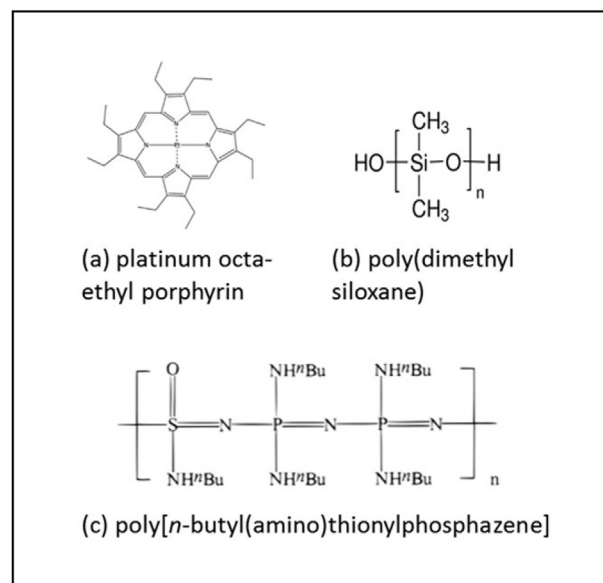


**Fig. 1.** Chemical structures of the phosphorescent dye (a) platinum octa-ethyl porphyrin (PtOEP), and the polymers (b) poly(dimethyl siloxane) (PDMS) and (c) poly[n-butyl(amino)thionylphosphazene] (C4PTP) investigated in this work.

system comprising a stack of micro-scale compartments to represent the polymer bulk, and source and receiver compartments separated by 1-nm-thick interfacial regions from the membrane. The construction of the reaction-diffusion model is described in Section 3.

### 2.2. Molecular dynamics simulations

In most continuum models, gas uptake and desorption at the surface of a polymer membrane are considered to be instantaneous, with bulk transport being the controlling factor in permeation rate. However, to build a predictive model, it is necessary to use physically-derived rate constants for all processes. The dynamics of gas-rubbery polymer collisions are not well studied, so we have selected CO<sub>2</sub> among the gases used in this work, N<sub>2</sub>, O<sub>2</sub>, CH<sub>4</sub>, and CO<sub>2</sub>, for a thorough investigation of the uptake process using molecular dynamics (MD) simulations. All of the gases are weakly interacting with the polymers they permeate, so we assume that the sticking coefficient obtained from the study of CO<sub>2</sub> can be applied to all the gases studied in this work.

Simulations are performed using the Desmond MD simulation package [18–20] and the OPLS-2005 force field [21]. A time-step of 1 fs is used for short-range interactions and a 3 fs time-step is used for long-ranged interactions. Long-ranged electrostatics are computed using the Ewald summation. A short-ranged Coulomb cutoff of 9 Å is used. Center of mass motion is removed at each time step in the adsorption simulations.

The initial PDMS structure is generated using standard protocols in polymer construction. The initial low-density ( $\rho = 0.0245 \text{ kg/m}^3$ ) structure is created using an amorphous builder. This polymer structure has 25 chains of PDMS of 100-monomer length, for a total of 25,053 atoms. To ensure that there are no overlapping atoms in the structure, 100 steps of energy minimization and 10 ps of dynamics in the NVT ensemble [22] at 10 K are performed (using a time constant of 0.1 ps for the thermostat). The density of the structure is increased by running 500 ps of dynamics in the NPT ensemble using the algorithm of Martyna, Tobias, and Klein (MTK) with a 1 ps time constant for the barostat [23]. To ensure

entanglement of the polymer chains, a Scaled Effective Solvent (SES) [24] equilibration step is performed in which long-ranged van der Waals and Coulomb interactions scaled to 20% of their original values, and dynamics are run for 2000 ps in the NVT ensemble with a Nosé-Hoover thermostat. Finally, with van der Waals and electrostatic interactions at their full strength, energy minimization is performed for 300 ps and the lattice parameters of the structure are again relaxed with 200 ps of NPT dynamics.

The above procedure results in a roughly 70 Å thick slab of PDMS created with dimensions of  $6.79 \times 6.79 \times 6.79 \text{ nm}^3$ . This procedure results in a bulk density of  $\approx 0.985 \text{ kg/m}^3$ , which is above the experimental reference value of  $0.970 \text{ kg/m}^3$  [25], but below the experimental sample densities of  $1.06\text{--}1.08 \text{ kg/m}^3$  obtained in this study (see Section 2.3.). To create a PDMS surface, the length of the cell is increased by 200 Å in the x-direction to generate a region of empty space. All polymer chains are kept intact. The surface is then equilibrated for 3000 ps in the NVT ensemble using the Berendsen thermostat at 300 K. The density near the surface is reduced to  $\approx 0.94 \text{ kg/m}^3$  due to surface roughness. The instantaneous surface is designated using the Gaussian smoothing method of Willard and Chandler [26], which is described more fully in the SI Section 1. The final, equilibrated structure and its instantaneous surface are shown in Fig. 2.

CO<sub>2</sub> absorption, adsorption, and desorption events are tracked using a procedure based on the molecular adsorption studies of Julin et al. [27,28]. A CO<sub>2</sub> molecule is introduced at a distance of approximately 15 Å from the surface and is assigned a velocity from the Maxwell-Boltzmann distribution at 300 K, with the constraint that the x-component of the velocity vector lies within a 45-degree cone normal to the surface. After 100 ps of NVE simulation, the outcome (adsorption, absorption, desorption) is recorded based on the position of the CO<sub>2</sub> molecule relative to the surface region, which is defined as points within 4 Å, i.e. twice the van der Waals radius, of the instantaneous surface. Justification of the 4 Å cutoff is given in the results section.

### 2.3. Experimental permeation measurements

Complete time-dependent permeation curves for several gases through PDMS were obtained in this work. To our knowledge such data have not been previously reported, and they are needed for accurate model construction and validation. Additional details are presented in the SI Sections 2 and 3.

**Sample Preparation.** PDMS samples are prepared using standard procedures. The PDMS base and a proprietary crosslinker (Sylgard

184, Dow Corning Corp., Auburn, MI) are mixed in a 10:1 ratio by weight. The PDMS solution is degassed to remove air bubbles and cast onto silicon wafers to the desired thickness via the spin-coating method. The polymer films are stored in deionized water until use. Prior to measurement, each sample is thoroughly dried and degassed. The thickness of the dry films is in the range of 163–165 μm, as measured by a micrometer (Mitutoyo, Aurora, IL). A helium gas displacement pycnometer (AccuPyc II 1340 from Micromeritics Instrument Corp., Norcross, GA) is used to measure the density, which ranges from 1.06 to 1.08 kg/m<sup>3</sup>. The glass transition temperature is  $149 \pm 0.3 \text{ K}$ , measured using differential scanning calorimetry (DSC800 Perkin Elmer, Waltham, MA).

**Gas Permeation.** A custom-built system is used for constant-volume gas-permeation experiments. A schematic is available in Reference [29]. Prior to the permeation experiment, gas is evacuated from the entire apparatus, a check for leaks is performed, and the measured permeabilities are corrected for any small pressure drifts. Upstream pressures of 119–835 kPa are tested. The upstream pressure is maintained at least two orders of magnitude greater than the downstream pressure during the measurements so that the pressure difference across membrane is effectively constant. The upstream pressure is monitored using a Honeywell STJE (Honeywell, Morris Plains, NJ) pressure transducer, which has a range of  $-2$  to 7000 kPa and an accuracy of  $\pm 100 \text{ kPa}$  [30]. The downstream pressure is monitored using a Baratron MKS (MKS Instruments, San Jose, CA) pressure transducer, which has a range of 0.1–1000 Pa and an accuracy of  $\pm 7 \text{ Pa}$  [31]. The temperature of the system is maintained at 308 K in a water bath using an Alpha immersion thermostat (Lauda, Delran, NJ). All gases, N<sub>2</sub>, O<sub>2</sub>, CH<sub>4</sub>, and CO<sub>2</sub>, (Praxair, Danbury, CT) are at least 99.9% pure and are used as received.

After the gas permeation process has reached steady state, the gas permeability of the membrane,  $P_m$ , is calculated from the gas flux,  $J$ , through membrane of thickness,  $l$ , due to a difference in partial pressure,  $\Delta p$ , across the membrane:

$$P_m = \frac{J l}{p_{up} - p_{ds}} = \frac{V_{ds} l}{\Delta p A R T} \left[ \left( \frac{dp_{ds}}{dt} \right)_{ss} - \left( \frac{dp_{ds}}{dt} \right)_{leak} \right] \quad (1)$$

where  $V_{ds}$  is the downstream collection volume,  $A$  is the membrane area,  $R$  is the universal gas constant,  $T$  is the temperature,  $p_{ds}$  refers to the downstream pressure,  $p_{us}$  refers to the upstream pressure, and  $(dp_{ds}/dt)_{ss}$  is the steady-state pressure rise, which is corrected for the leak rate  $(dp_{ds}/dt)_{leak}$ . At steady state,  $P_m = D \times S$ .

### 3. Development of a kinetic model for O<sub>2</sub> sorption and phosphorescent dye quenching in a sensor system

Detailed reaction-diffusion models for non-steady state transport in polymer membranes have not been reported previously, and development of a predictive description requires multiple independent types of time-dependent experimental measurements to validate it [12,14]. There are few of these in the literature for any polymer type, however, a particularly useful set for rubbery polymers has been reported by Jayarajah and coworkers [6,7]. In this section, we describe how we developed the model for their measurements, quenching of a phosphorescent dye in a rubbery polymer by oxygen for a sensor application [8], and compared predictions to experimental observations. The polymer used is poly(*n*-butyl (amino) thionyl phosphazene) (C4PTP). This polymer has a low T<sub>g</sub> of 257 K and was studied at a thickness of 163 μm. The dye platinum octa-ethyl porphyrin (PtOEP) is dispersed in the polymer, and quenching of its laser-excited phosphorescence acts as an indicator of the internal concentration of O<sub>2</sub> gas. The structures of the C4PTP monomer and of PtOEP are shown in Fig. 1 and

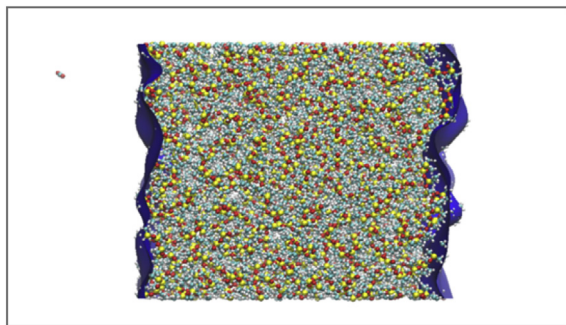


**Fig. 2.** The structure of poly(dimethyl siloxane) (PDMS) in the molecular dynamics simulations. Hydrogen atoms are shown in white, carbon in light blue, oxygen in red and silicon in yellow. The instantaneous interface is shown in dark blue. The CO<sub>2</sub> molecule (upper left hand corner of the image) is sent towards the surface of the PDMS polymer structure for an adsorption simulation. (For interpretation of the references to colour in this figure legend, the reader is referred to the web version of this article.)

the reaction mechanism and rate coefficients are summarized in Table 1.

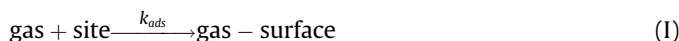
### 3.1. System geometry

As shown in Fig. 3, the membrane is represented as a set of 100 homogeneous compartments, each 1.63  $\mu\text{m}$  thick, coupled by Fickian diffusion paths. An interfacial compartment of 1 nm thickness is provided at the gas-polymer interface to enable explicit description of adsorption, desorption and transfer of gases to and from the polymer bulk. The other side of the membrane is in contact with a glass substrate and so is not permeable. The area of the membrane is taken to be the footprint of the laser beam used for dye excitation, 2 mm by 1 mm.

### 3.2. Gas-polymer interactions

The experimental diffusion coefficient is used for gas transport throughout the polymer, including the surface layers. The maximum concentration of a gas in the membrane is determined by its experimental Henry's Law solubility. Swelling was not reported for this system and is neglected in the simulations. When present, dynamic volume changes as the membrane swells must be included in the model. They will reduce solute concentrations and concentration gradients while increasing the diffusion coefficient, and their effect on permeation may vary with time.

Adsorption and desorption are represented as direct processes involving a gas molecule and a surface site, a description used in other studies [15]. Adsorption is broken into two steps: sticking of the gas to the membrane surface and diffusion from the surface layer into the bulk. Sticking is represented as a reaction between a gas molecule and an empty surface site,



where the adsorption rate constant,  $k_{\text{ads}}$ , is the collision frequency of the gas with the surface,  $k_{\text{coll}}$ , times the sticking probability,  $\mu$ ,

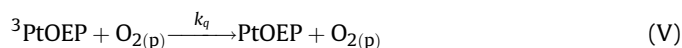
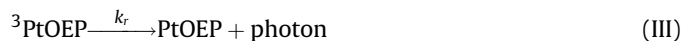
$$k_{\text{ads}} = \mu k_{\text{coll}} = \mu (ZA) = \mu \left( \frac{p_{\text{up}}}{\sqrt{2\pi m_w k_B T}} \right) A \quad (\text{2})$$

and  $Z$  is the collision frequency per unit area,  $A$  is the experimental surface area,  $p$  is the upstream partial pressure of the gas,  $m_w$  is the molecular mass of the gas,  $k_B$  is Boltzmann's constant, and  $T$  is the temperature [34]. The sticking coefficient is initially assumed to be 0.1 (which is high but not unity since there is no information in the

literature for this system); the sensitivity of the simulation to this value has been investigated and will be discussed in a later section. We use the generic term “site” because we assume that the gas molecules can physisorb to an atom type at the surface. The concentration of surface sites is assumed to be that of surface atoms in a liquid,  $10^{14}$  atoms/cm<sup>2</sup> [35]. Since the surface must be represented in a 3-dimensional compartment in Kinetiscope, the sites are distributed through a 1-nm thickness, giving a concentration of 1.66 mol/L. Once adsorbed, the gas molecule can diffuse from the interface layer to the adjacent bulk polymer compartment. Desorption from the membrane is represented as detachment from a surface site, the reverse of Reaction I. Because the polymer and gas molecules are weakly interacting, we base the desorption rate constant on the breaking of a single van der Waals bond in the gas phase, such that  $k_{\text{des}} = 1.4 \times 10^{11} \text{ s}^{-1}$  [36,37]. The sensitivity of the simulation results to assumptions concerning the surface description is discussed below.

### 3.3. Kinetics of dye quenching

The dye is assumed to be uniformly distributed throughout the polymer bulk, and its excitation and deexcitation reactions are:



where PtOEP is in the ground state,  $^3\text{PtOEP}$  is in the first excited triplet state, and  $\text{O}_{2(\text{p})}$  is the oxygen gas within the polymer phase. These steps are the non-radiative decay, radiative decay, triplet-triplet annihilation (TTA), quenching, and excitation steps, respectively. In this section, we describe how the rate constants have been determined for these steps.

The photophysics have been determined from studies on PtOEP in polymer environments [6,7,33,38]. From the ground state, PtOEP absorbs at 380 nm and 547 nm to enter the first excited state [38]; greater than 99.9994% of PtOEP molecules excited to the first singlet state undergo intersystem crossing to the first excited triplet state  $^3\text{PtOEP}$  [33]. Therefore, fluorescence from the singlet state is neglected.  $^3\text{PtOEP}$  emits at 647 nm when well-dispersed in a clear polymer [33,38]. For excited-state dye at high concentration or in solution with low viscosity, TTA may occur, in which one  $^3\text{PtOEP}$  molecule quenches another and is itself excited back to the first excited singlet state. Because each excited singlet quickly relaxes to the first excited triplet we do not explicitly track the first excited singlet state in Reaction IV [33].

Two types of experiments are examined to construct and validate a kinetic model for PtOEP photoprocesses. One determines the dye's phosphorescence lifetime using pulsed laser excitation [33,38]; the other determines the emission intensities of oxygen-free and oxygen-saturated polymer under continuous laser excitation [7].

#### 3.3.1. Dye lifetime by pulsed laser excitation

**Oxygen-free Environment.** The phosphorescence lifetime,  $\tau_0$ ,

**Table 1**  
Simulation inputs for phosphorescence quenching.

	units	PS	Ref.	C4PTP	Ref.
$D(\text{O}_2)$	$\text{m}^2/\text{s}$	$1 \times 10^{-11}$	[32] <sup>a</sup>	$4.0 \times 10^{-10}$	[7]
$S(\text{O}_2)$	$\text{mol}/(\text{L Pa})$	$8.26 \times 10^{-8}$	[32] <sup>a</sup>	$1.18 \times 10^{-8}$	[7]
$[\text{O}_{2(\text{p})}]_{\text{eq}}$	$\text{mol}/\text{L}$	$1.73 \times 10^{-3}$	this work	$2.40 \times 10^{-4}$	this work
$[\text{PtOEP}]$	$\text{mol}/\text{L}$	0.0731	[33]	$3.1 \times 10^{-4}$	[7]
$[\text{ } ^3\text{PtOEP}]_{\text{init}}$	$\text{mol}/\text{L}$	$5.85 \times 10^{-4}$	this work	$2.48 \times 10^{-6}$	this work
$\Phi_{\text{P}}$		0.54	[33]	0.54	this work
$\tau_0$	$\mu\text{s}$	60	[33]	103	[7]
$k_{\text{r}}$	$\text{s}^{-1}$	$8.33 \times 10^3$	[33]	$3.9 \times 10^3$	this work
$k_{\text{nr}}$	$\text{s}^{-1}$	$8.30 \times 10^3$	[33]	$5.8 \times 10^3$	this work
$k_{\text{TTA}}$	$\text{M}^{-1} \text{ s}^{-1}$	$4 \times 10^7$	[33]	$4 \times 10^7$	this work
$k_{\text{q}}$	$\text{M}^{-1} \text{ s}^{-1}$	$1.82 \times 10^7$	this work <sup>b</sup>	$3 \times 10^9$	this work
$k_{\text{ex}}$	$\text{s}^{-1}$	—		50	this work

<sup>a</sup> For amorphous, atactic polystyrene.

<sup>b</sup> Calculated from the reported pseudo-first order rate constant  $3.20 \times 10^4 \text{ s}^{-1}$  reported in Ref. [33] and the expected concentration of  $\text{O}_2$  in the polymer.





constants for all decay processes in the dye kinetics scheme are fixed, simulation of the emission intensity can be used to determine  $k_{ex}$ . However, the experimental data are reported as relative intensity values, rather than absolute intensities. The extrema in intensities are captured in the ratio  $B = I_0/I_{eq} - 1$ , where  $I_0$  is the phosphorescence intensity in the absence of oxygen, and  $I_{eq}$  is the intensity for a constant concentration of  $O_2$  consistent with  $p_{O_2} = 21$  kPa. The experimental value is  $B = 74 \pm 6$ . Simulations of the oxygen-free and oxygen-saturated steady-state scenarios are performed; then absolute and relative intensities are calculated. Values for the relative intensity  $B$  are plotted as a function of  $k_{ex}$  in Fig. S3 in SI Section 6. The value of the ratio is quite insensitive to  $k_{ex}$  over a range of 1–100 s<sup>-1</sup>, where  $B$  stays between 65 and 67. The median of  $k_{ex} = 50$  s<sup>-1</sup> is chosen, at which  $B = 66$ .

### 3.3.3. Time-dependent data

The intensity over time,  $I(t)$ , was used by Jayarajah et al. to determine the solubility coefficient,  $S$ , and the diffusion coefficient,  $D$ , for  $O_2$  in C4PTP using a two-parameter fit to the equation,

$$I(t) = \frac{I_0}{l} \int_0^l \frac{[O_{2(p)}]_{eq}}{1 + B [O_{2(p)}](x, t)} dx \quad (7)$$

where

$$B = \frac{I_0}{I_{eq}} - 1 = 4 \pi N_{Av} \tau_0 R_{AB} D S p_{O_2} \quad (8)$$

where  $l$  is the membrane thickness,  $N_{Av}$  is Avogadro's number,  $\tau_0$  is the lifetime of PtOEP in the polymer environment in the absence of oxygen,  $[O_{2(p)}](x, t)$  is the absolute concentration of  $O_2$  within the membrane at position  $x$  at time  $t$ , and  $[O_{2(p)}]_{eq}$  is the equilibrium concentration of  $O_2$  within the membrane, which is equal to  $S \times p_{O_2}$  [6,7,39]. The equation above assumes that the dye is both distributed and excited homogeneously throughout the membrane (i.e. the sample is optically thin). In the simulations, we also use a homogeneous dye distribution and assume homogeneous excitation.

The continuous excitation experiments were performed in two modes: (i) sudden replacement of  $N_2$  with air, leading to sorption of  $O_2$  and a decay in phosphorescence intensity, and (ii) sudden replacement of air by pure  $N_2$ , leading to desorption of  $O_2$  and an increase in phosphorescence intensity. Because the pressure vs time data are not available to use as input to the simulations, the increase or decrease in oxygen partial pressure is assumed to be instantaneous in the simulation.

## 4. Simulations of the $O_2$ sensor system

Simulations of emitted light intensity as  $O_2$  sorbs into or desorbs from the polymer are used to calculate  $I(t)$  for comparison to experimental data. The absorption and desorption simulation results are compared with the experimental data in two ways: (i) dye kinetics are not simulated directly, but the total amount of  $O_2$  predicted to be absorbed in the polymer in the simulation is used to calculate the expected  $I(t)$  using the reported intensity ratio of  $B = 74$  and Equations (7) and (8), and (ii) full simulation of the dye kinetics and the photons produced per unit time are directly compared to the experimental intensity over time. The use of two methods serves as a check on the internal consistency of the experimental data and on the validity of the reaction mechanism. The experimental value of  $B$  is chosen for comparison in method (i) because the estimation of  $k_{ex}$  introduces an additional discrepancy between simulation and experimental results.

The simulations predict the amount and distribution of oxygen

gas within the membrane at all times. We compare the simulated  $O_2$  amount to experiment, which does not measure  $O_2$  in the film directly, by calculating  $n$ , the expected amount of  $O_2$  in the membrane, from the experimental  $I(t)$  curve. We assume  $dx = l$  in Equation (7), i.e. that the film is entirely uniform. The maximum amount of  $O_2$  in the membrane,  $n_{max}$ , is found at equilibrium.  $n_{max} = [O_{2(p)}]_{eq} \times V$ , where  $V = A \times l$ . Then, rearranging Equations (7) and (8) gives

$$n = n_{max} \frac{1}{B} \left[ \frac{B+1}{I(t)} - 1 \right] \quad (9)$$

Simulation results for sorption and desorption are compared to experiment in Fig. 5. The shape of the calculated curves is in good agreement with observations, but there are several quantitative differences. The initial rise in the simulated amount of  $O_2$  in the polymer shown in Fig. 5b is faster than that calculated from the experimentally measured  $I(t)$  using Equation (9). In the simulation, the amount of  $O_2$  in the membrane compartments near the gas-polymer interface increases rapidly, and they become saturated with  $O_2$ . The rate of  $O_2$  absorption then slows, limited by  $O_2$  diffusion to the other side of the membrane. The reason for the difference between simulated and experimental amount of  $O_2$  is unclear. One possibility is that the assumption of  $dx = l$  in the calculation of the amount of  $O_2$  from  $I(t)$  (either experimental or simulated) is not valid, which is supported by the fact that simulated and measured  $I(t)$  curves are in much closer agreement (Fig. 5a).

Another possibility is the presence of inhomogeneities either in the polymer, dye distribution, or emission, that would lead to the same total phosphorescence intensity but no simple relationship between light emission and total  $O_2$  in the film. This possibility was tested in two ways. First, a simulation in which dye is not present in the top quarter of the membrane gives a similar  $I(t)$  curve to experiment, showing that emission intensity is insensitive to spatial distribution of the dye and therefore to details of the  $O_2$  kinetics. Second, altering the pressure profile of  $O_2$  so that it does not instantaneously rise to  $p_{O_2} = 21$  kPa, but rather increases over several seconds, which is more similar to the experimental procedure, does not change the shape of the curve. Finally, the assumption that the sample is optically thin is tested via simulation in which only the dye in the top half of the membrane becomes excited; this situation results in an intensity profiles that dies off much more quickly than experiment. These considerations suggest that Equations (7) and (8) are qualitatively valid for estimating the full time dependence of  $O_2$  absorption, but may not be quantitative in all cases.

Comparison of Fig. 5a and c and Fig. 5b and d also shows that while phosphorescence decays rapidly, the  $O_2$  concentration in the membrane does not reach saturation until much later. In the sorption simulations,  $O_2$  starts to reach the membrane compartments furthest from the interface after 2.0 s. The concentration of  $^3PtOEP$  is very small, and is fully quenched 8.1 s after the introduction of  $O_2$  to the polymer. However, the concentration of  $O_2$  continues to rise for another 140 s. Thus, there is not a one-to-one correspondence between the intensity and the  $O_2$  concentration in the sensor film outside the range of 1–50  $\mu\text{mol/L}$  of  $O_2$ , or an external partial pressure of 2–130 Pa, far below that used in this experiment.

The shape of the  $I(t)$  desorption curve for C4PTP is also captured well by the simulation (Fig. 5e). There is an initial small but rapid increase in  $I(t)$  because the  $O_2$  in the top membrane compartments desorbs in the first few seconds. From then until 50 s, there is slower rise in intensity as  $O_2$  diffuses from the lower compartments and desorbs, but the overall  $O_2$  concentration within the membrane

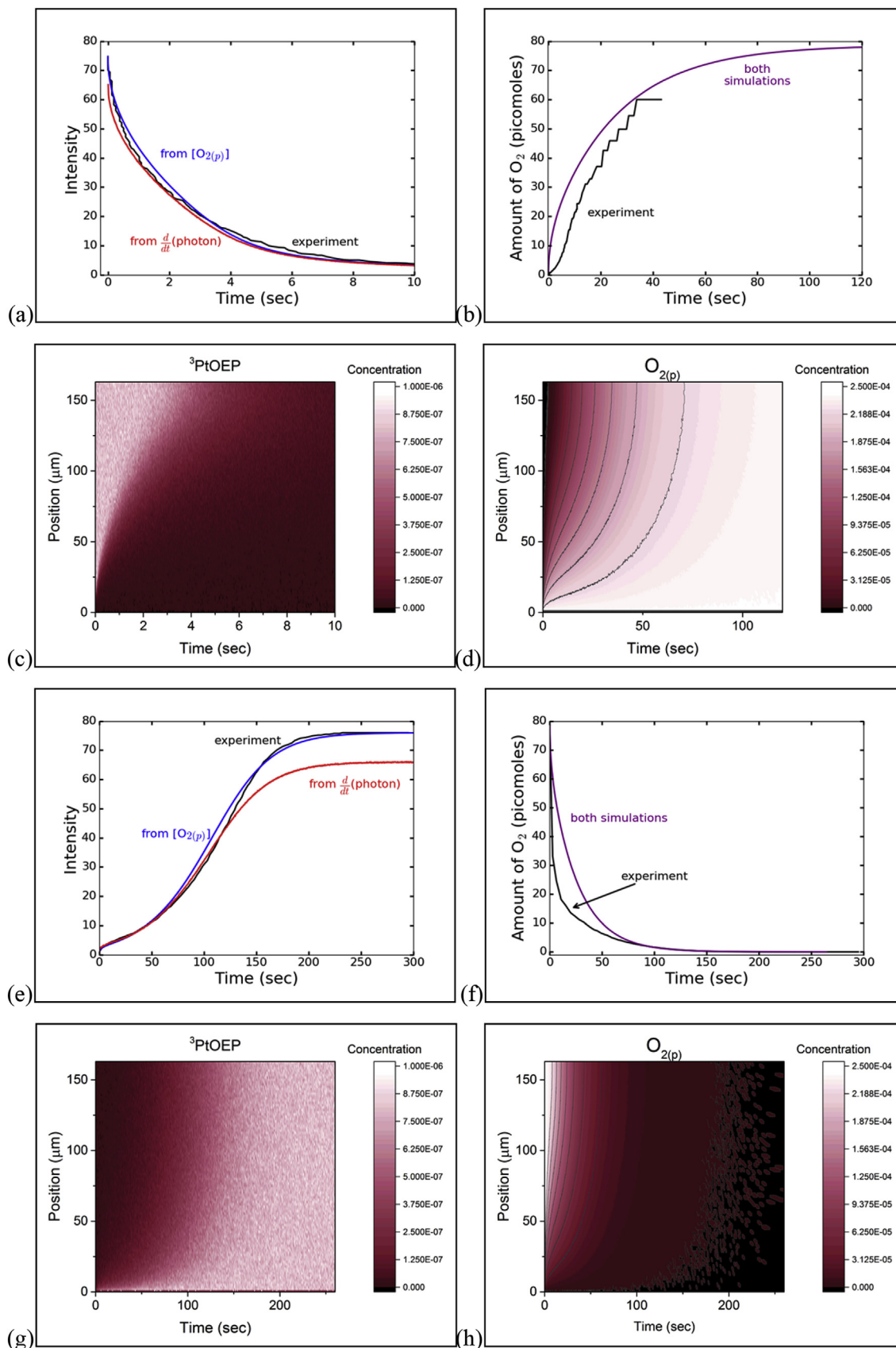


**Fig. 5.** Results of simulation of laser-excited PtOEP and  $O_2$  kinetics in C4PTP. In all the contour plots, darker colors represent lower concentration, and lighter colors represent higher concentration. Position is defined as 0 at the gas interface of the polymer. (a)  $I(t)$  when  $O_2$  sorbs into the polymer, calculated from  $O_{2(p)}$  with Equations (7) and (8) (blue) and from direct simulation of the dye photophysics (red); (b) The amount of  $O_{2(p)}$  in the polymer as a function of time, comparing that calculated from the experimental data and both



is still high enough to quench most of the dye. A more rapid increase in intensity ensues after 50 s, once the  $O_2$  concentration is no longer in excess of that needed to quench  $^3\text{PtOEP}$ . Finally, the maximum intensity is reached around 200 s, once all of the  $O_2$  is removed from the polymer. The contour plots shown in Fig. 5g and h, support this interpretation. The simulated  $O_2$  content shown in Fig. 5f is higher than that extracted from the  $I(t)$  measurements. This discrepancy may have the same origin as discussed above for the sorption case, Fig. 5b.

Sensitivities of the simulation results to uncertainties have been thoroughly evaluated. Those for  $D$  and  $S$  are discussed in the SI Section 7 and shown in Fig. S4. Those of the assumed properties of the gas-polymer interface are presented in Figs. S5 and S6 and summarized here. Saturation of surface sites by  $O_2$ , assuming a sticking coefficient of 0.1, occurs within  $10^{-21}$  s at 21 kPa. Reduction of the sticking coefficient to  $10^{-17}$  has no effect on the  $O_2$  profile, nor does increasing the sticking coefficient to 1. The concentration of adsorption or desorption sites can also be varied by 1–2 orders of magnitude with no effect. Alteration of the surface diffusion coefficient does not change the sorption results. Reduction, though not increase, of the interfacial diffusion coefficient does alter the desorption results, however. Finally, the desorption rate constant can also be reduced or increased by several orders of magnitude without altering the oxygen profiles. Because the simulation results are largely insensitive to surface kinetics at the rubbery polymer-inert gas interface, this type of simulation is not useful for exploring them, therefore we have used molecular dynamics simulations to gain more insight into the processes occurring at the surface.

## 5. Permeation of gases through a membrane separator: experiment and simulations

Having established a suitable reaction-diffusion framework as described in the preceding sections, we use it to examine the fully time-dependent permeation data obtained in this work, capturing not only steady-state permeation, but also the downstream pressure rise for steady-state and pre-steady-state regimes. In this section, we present the permeation measurements and simulations of them. In view of the insensitivity of sorption of gas by rubbery polymer sorption to assumptions of gas sticking, we report molecular dynamics calculations to provide a description of this process for one system, thus avoiding an arbitrary guess in the model.

### 5.1. Measurements of time-dependent permeation through PDMS

In this study, the permeation of the gases  $N_2$ ,  $O_2$ ,  $CO_2$ , and  $CH_4$  through PDMS is investigated at 308 K for various pressure gradients. The set of all experimental data is summarized in Table S1. The pressure vs time data are presented in the SI Section 8, and a selection of data is shown in Fig. S7. The permeability is calculated from the rate of pressure increase downstream from the membrane when steady state is reached; differences due sample to sample variations are accounted for in the calculation of permeation via Equation (1). The permeability values as a function of pressure difference between source and receiver volumes are given in Fig. 6. Each data point represents an average value of three or more different samples and measurements. The leak rate for each

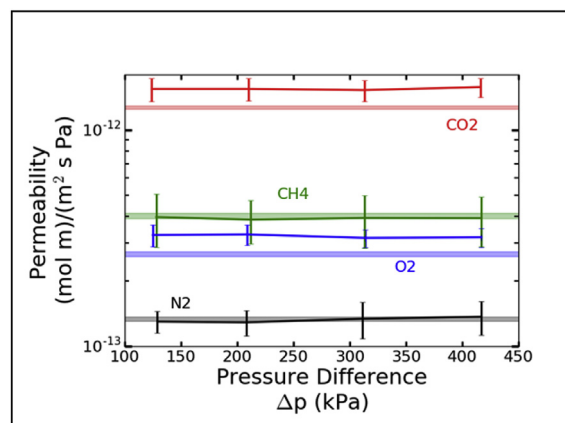


Fig. 6. Comparison of experimental permeability to literature values. The literature values from Ref. [40] are shown with their standard deviation as the shaded regions.

measurement is kept under 0.05% of the permeate flux. Propagated measurement error ranges from 1 to 4%. The error bars show the sample-to-sample variability, which is 10–20%. As can be seen in Fig. 6, permeability shows no dependence on pressure gradient, indicating that the sorption isotherm is also linear. Permeation values for PDMS can vary with changes in base to cross-linker ratio, casting method, and annealing temperature. The measured values are consistent with previously measured values within experimental error and the sample-dependent variability of literature values [40–42]. Higher pressure gradients (600–850 kPa) were also investigated, but with fewer experiments such that the variation between samples was not robustly characterized; so these data are omitted from Fig. 6.

### 5.2. Calculation of sticking probability of $CO_2$ on PDMS

Few data are available on sticking coefficients to of weakly interacting gases to PDMS or other rubbery polymers; therefore, we use molecular dynamics simulations to estimate reasonable values. We found that the sticking process is not kinetically limiting during construction of the permeation model for PDMS, similar to the finding for  $O_2$  in C4PTP, so we have performed calculations for a single gas,  $CO_2$ , and assume that its sticking coefficient on PDMS is applicable to the other gases investigated. A series of 250 simulations of  $CO_2$  impacts onto a PDMS surface was performed, and the results are shown in Fig. 7 and summarized in Table 2. Some care must be taken in how the classification of type of event is interpreted: the distinction between an adsorbed and absorbed molecule is arbitrary, especially for atoms just below the interface, and the fate of molecules adsorbed on the surface is not clear from the finite simulation time. Thus, sticking in these simulations has a lower bound of 30%, equal to the fraction of absorbed molecules, and an upper bound of 50%, equal to the fraction of absorbed plus adsorbed molecules. The minimum sticking coefficient of 30% is used in the reaction-diffusion simulations for all gas molecules.

The most similar system that has been studied experimentally is the scattering of the  $O_2$  gas from the surface of the hydrocarbons squalane and dodecane [43]. At incident energies of 8 kJ/mol, twice

simulation types; (c) Contour plot of the concentration of  $^3\text{PtOEP}$  through the polymer thickness during 10 s of sorption, showing complete quenching of phosphorescence; (d) Contour plot of the concentration of  $O_{2(p)}$  through the polymer thickness, reaching saturation after 120 s of sorption. (e)  $I(t)$  when  $O_2$  desorbs from the polymer, calculated from  $O_{2(p)}$  with Equations (7) and (8) (blue) and from direct simulation of the dye photophysics (red); (f) The amount of  $O_{2(p)}$  in the polymer as a function of time, comparing that calculated from the experimental data and both simulation types; (g) The concentration of  $^3\text{PtOEP}$  through the polymer thickness over time during desorption, with recovery of uniform phosphorescence by 200 s; (h) The concentration of  $O_{2(p)}$  through the polymer thickness over time during desorption, uniformly reaching zero between 200 and 250 s. (For interpretation of the references to colour in this figure legend, the reader is referred to the web version of this article.)

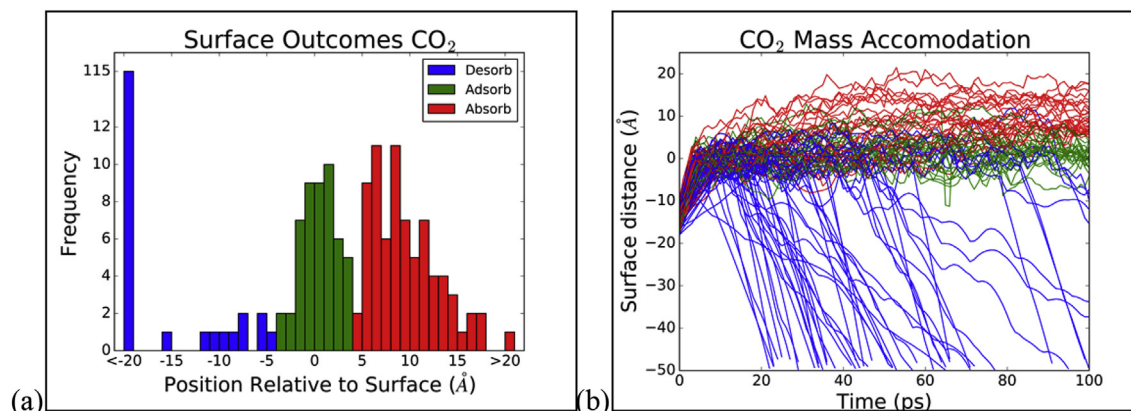


**Fig. 7.** Results of molecular dynamics simulations for CO<sub>2</sub> sticking to PDMS. The surface is defined as position 0 with positive position indicating the region occupied by polymer and negative position indicating the empty region. Absorbed molecules are plotted in red, adsorbed molecules in green, and scattered and desorbed molecules in blue. (a) Histogram showing the distribution of outcomes from all 250 simulations. Note that the far left blue bar represents desorption in 115 simulations. (b) Distance from the final Willard surface as a function of time for 100 randomly selected trajectories. (For interpretation of the references to colour in this figure legend, the reader is referred to the web version of this article.)

**Table 2**  
Results of Molecular Dynamics study of sticking of CO<sub>2</sub> to a PDMS surface.

Events	Absorb	Adsorb	Desorb	Total
Number	75	50	125	250
Percent	30	20	50	100

the average kinetic energy for gas molecules in this study, the oxygen molecules fully transfer their excess energy to the hydrocarbon surface [43], indicating a sticking probability near 100%. A MD study of carbon dioxide [44] colliding with hydrocarbon self-assembled monolayers (SAMs) also shows a large sticking probability of  $\approx 70\%$  when the SAMs are terminated with  $-\text{CH}_3$  or  $-\text{OH}$  functional groups. The sticking probability falls to  $\approx 40\%$  for SAMs terminated with  $-\text{CF}_3$ . The reason for such a high sticking probability is explained in a MD study of argon colliding with hydrocarbon SAMs terminated with  $-\text{CH}_3$  and  $-\text{CF}_3$ . The SAMs terminated with  $-\text{CH}_3$  are able to redistribute the energy of the incoming molecule on the same timescale as the impact of the atom with the surface by recruiting a large number of low-frequency (inter-chain) vibrational modes; the SAM's terminated with  $-\text{CF}_3$  redistribute the energy more slowly along high-frequency (intra-chain) vibrational modes, resulting in a lower sticking probability [45]. PDMS contains a large number of low-frequency interactions, and so an energy transfer mechanism similar to  $-\text{CH}_3$  terminated SAMs may apply. Thus, we conclude that a sticking probability of 30–50% is reasonable for a light, inert gas molecule at ambient temperature colliding with a flexible polymer surface. Further study of this type of system, and systems in which there are stronger interactions between the gas and the polymer, would be useful.

The absorption mechanism observed in the MD simulations involves CO<sub>2</sub> interacting with a gap between the polymer chains during a gas-surface collision or while transiently physisorbed, and passing directly into the polymer bulk. The simulations did not show that CO<sub>2</sub> has a strongly preferred adsorption site, i.e. atom type, on the PDMS surface. This is expected for gas-polymer combinations with weak interactions and supports our assumption that every surface atom is an available binding site in the reaction-diffusion simulations. If strong hydrogen bonding were possible, the surface area available for adsorption would be reduced [46,47]. On the other hand, if roughness were significant the surface sites available would be greater than assumed. The MD simulations show that the ratio of the instantaneous surface area to the nominal

surface area is 1.1, indicating that the actual, rough, surface area is only 10% greater than the ideally smooth surface assumed in the reaction-diffusion simulations.

### 5.3. Simulations of time-dependent permeation

The model framework constructed for phosphorescence quenching (Fig. 3) is modified for PDMS permeation by removing the dye quenching kinetics and replacing the glass support with a gas collector volume. A 1 nm thick interfacial region is provided between the polymer and the gas collector, and the desorption steps occur therein; no desorption occurs at the upstream interface in the permeation simulations. The size of the collection compartment is set equal to the experimental collection volume of 41.3 cm<sup>3</sup>. The diffusion coefficient of desorbed gases from the interface into the collection chamber is 2.0 m<sup>2</sup>/s. The surface site concentration of 1.66 mol/L and the desorption rate constant of  $1.4 \times 10^{11} \text{ s}^{-1}$  are the same as above. The multi-scale simulation setup is shown in Fig. 8. Instrumental characteristics such as volumes and the measured pressure rise in the upstream chamber when gas is initially introduced are included in the model. Because the downstream volume remains at low pressure relative to the surroundings, a small amount of gas can leak into the collection chamber; this effect is included in the simulations for the sake of completeness. Details on the implementation of this step can be found in the SI Section 9, and relevant values are listed in Table S2.

The solubility of each gas in PDMS is taken from the literature [40]. The permeability measured under each experimental condition (combination of gas, polymer sample, and upstream pressure) is divided by the literature solubility to calculate the diffusivity. These experimental conditions and the values used in simulation are presented in Table 3. We use the literature value for solubility because solubility varies only over an order of magnitude for a given polymer, whereas the diffusivity within the polymer may vary over six orders of magnitude for different permeants [48]. Only N<sub>2</sub> and CO<sub>2</sub> are presented in the main body, since they represent the lower and upper limits of permeability in PDMS, respectively; similar data for O<sub>2</sub> and CH<sub>4</sub> are available in the SI. The adsorption rate constant is calculated for each  $p_{up}$  from Equation. (2) with  $\mu = 0.30$ .

Experimentally, the upstream permeant gas pressure  $p_{up}$  increases over several seconds after opening the gas valve. This rise is captured and used as an input to the simulation rather than assuming an instantaneous pressure step. The beginning of the rise

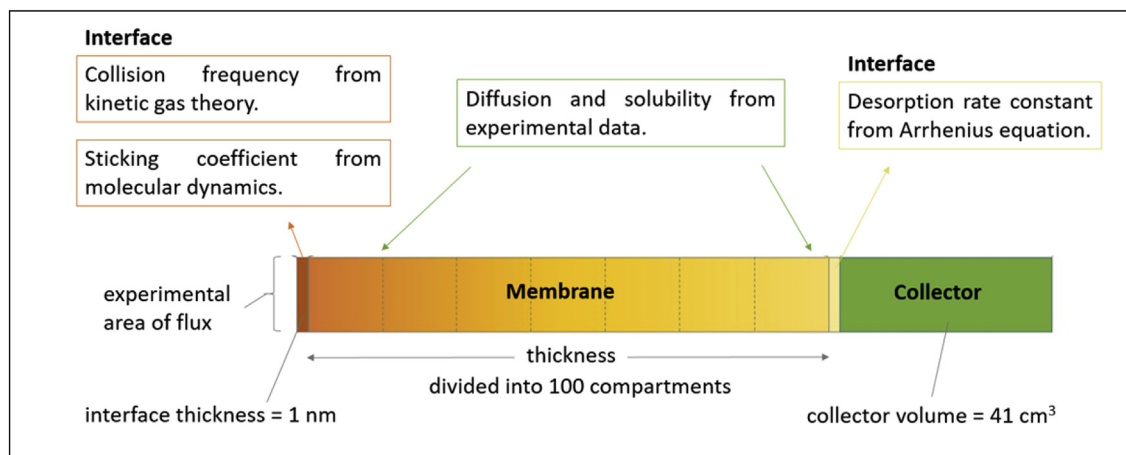


**Fig. 8.** Overview of multi-scale model for a permeation simulation. The membrane is divided into 100 compartments, plus two thin interfacial compartments. An additional compartment collects gas after its permeation. The thickness and area are based on the particular sample being simulated. The surface description is the same as for the dye quenching study, except for the sticking coefficient, which is now known from MD.

**Table 3**

Input values for multi-scale simulations for comparison to experimental permeation of PDMS.

Gas	$S^a$ mol/(L Pa)	Sample ID	$l$ $\mu\text{m}$	$A$ $\text{cm}^2$	$p_{up}$ kPa	$D$ $\text{m}^2/\text{s}$
$\text{CO}_2$	$5.68 \times 10^{-7}$	L4S2	163	0.203	122	$2.34 \times 10^{-9}$
					206	$2.34 \times 10^{-9}$
					311	$2.39 \times 10^{-9}$
$\text{N}_2$	$3.96 \times 10^{-8}$	L4S2	163	0.203	122	$3.27 \times 10^{-9}$
					206	$3.26 \times 10^{-9}$
					416	$3.26 \times 10^{-9}$
		L5S1	165	0.187	820	$2.80 \times 10^{-9}$

<sup>a</sup> Reference [40].

is used as the zero for the simulation time base. The changing internal concentration of the gas in the polymer is set to be proportional to the external pressure,  $p_{up}$ ,

$$[gas_{(p)}] = S p_{up} \quad (10)$$

where the proportionality constant,  $S$ , is the gas's Henry's law solubility over the pressure range in this study [40]. Figs. 9a–c and 10 show the permeation curves from experiment and the corresponding simulations for  $\text{N}_2$  and  $\text{CO}_2$ , respectively, through PDMS for upstream pressures from 122 to 820 kPa. While the experimental standard deviation for samples at higher pressures was not thoroughly investigated, the data are sufficient for comparison to simulation. The figures for  $\text{N}_2$  and  $\text{CO}_2$  are highlighted here because they represent the extremes in permeability among the gases tested; similar data for  $\text{O}_2$  and  $\text{CH}_4$  are available in the SI Section 11, Fig. S8 and Table S3. The agreement for all times, gas types, and pressures is within experimental error, confirming that the simulation framework and the model represent the full permeation process over a wide range of conditions, Henry's law solubilities, and permeabilities. More details on implementation of Equation (10) in the model are presented in the SI Section 10, and relevant values are listed in Table S2. The error introduced by ignoring the dynamic solubility increase is illustrated in Fig. 9d, in which the results of simulations with instantaneous and dynamic increases in available binding sites are compared. The simulation with a dynamic increase faithfully reproduces the pre-steady-state region of the permeation curve; the simulation with all binding sites instantly available only reproduces the steady-state region of the

curve. This dynamic treatment is especially important for the more permeable gases or where the upstream pressure rise takes place over a long time.

The simulations add two new insights to dynamical aspects of the system. First, we find that inclusion of instantaneous increases in the maximum possible concentration of the permeant in the membrane as the permeant pressure increases on the upstream side is required for good agreement between the experimental and calculated pressure rise for all gases studied. This behavior would need to be incorporated in any new theoretical treatment of solution-diffusion in membranes far from steady state. It should be noted that while the computational treatment for single permeants is straightforward, it is likely to be more complex when time-varying mixtures are involved. Second, we find that the bulk PDMS diffusion coefficient is sufficient to describe gas motion at all locations within the polymer. This indicates that tortuosity, polymer chain fluctuations, and other detailed, molecular-level characteristics are well-captured by the Fickian diffusion description, and do not need to be included explicitly.

## 6. Application of the model: predictive simulations for two rubbery membrane separations systems

Two variations of the reaction-diffusion framework developed in this work are used to develop models that account for the entire experimentally observed permeation process, both steady-state and pre-steady-state, for phosphorescence quenching, and gas permeation through a membrane. The models have no adjustable parameters and are physically realistic, and therefore predictive. In this section we take one of the models, gas permeation through PDMS, to examine two other types of systems at an exploratory level:  $\text{CO}_2$  separations from air, and solar  $\text{CO}_2$  photoelectrochemical reduction. We describe how the system models are set up, then present and discuss the predictions from the simulations.

### 6.1. Simulations of $\text{CO}_2$ separation from air

There is currently much interest in use of permeable membranes for  $\text{CO}_2$  capture from ambient air [49,50] and we use the PDMS permeation model described above to examine how a membrane with its properties would function. Experimentally, gases have been shown to permeate independently in rubbers [51,52]. Simulation of permeation of a mixture of  $\text{N}_2$  and  $\text{O}_2$ , using

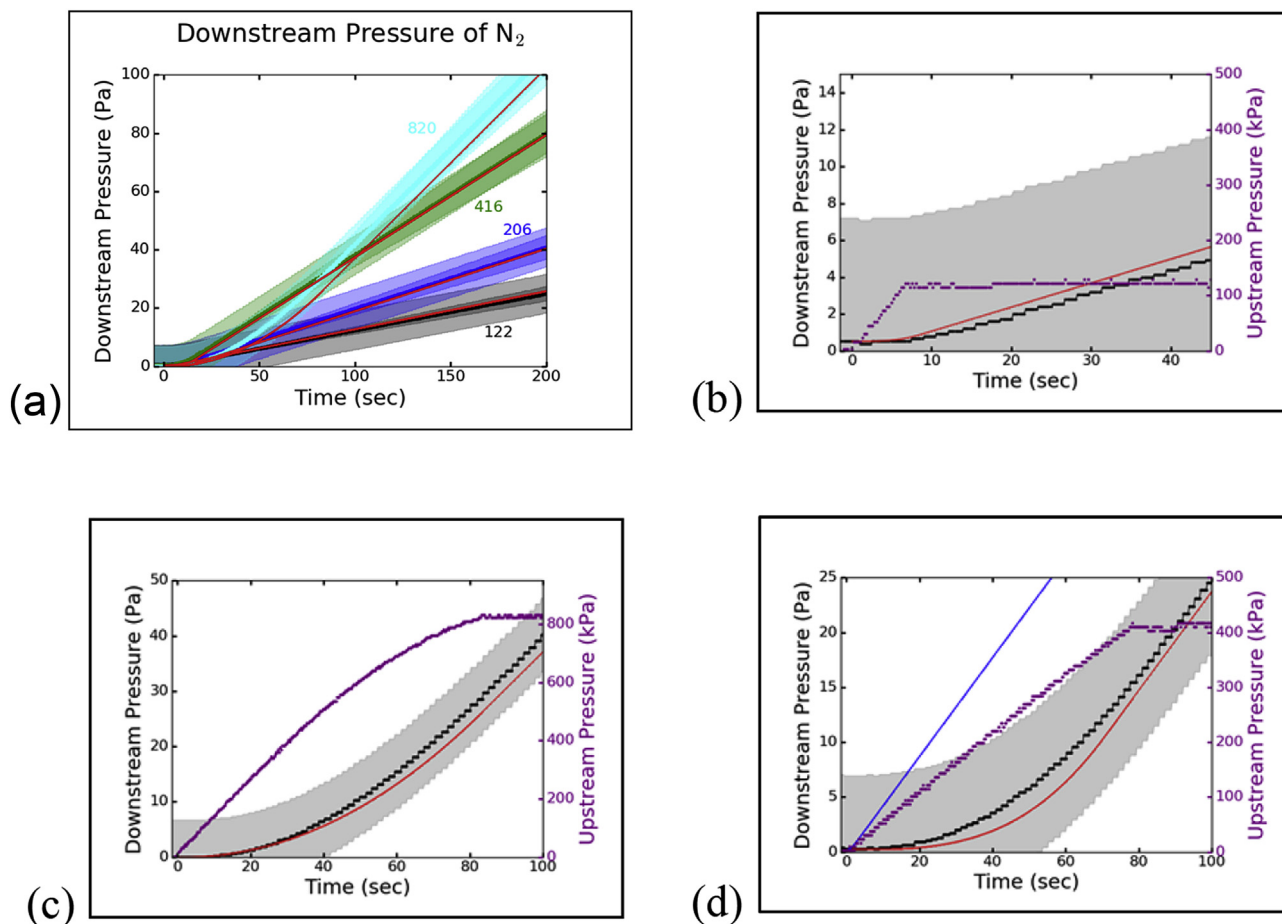


**Fig. 9.** Comparison of simulation and experimental permeation curves for  $N_2$ . The simulation results are shown in red. (a) Summary plot for all pressures. The shaded regions represent an experimental sample-to-sample standard deviation of 10%. Each curve is labeled with the upstream pressure in kPa. (b) Pre-steady state detail for  $p_{up} = 122$  kPa. (c) Pre-steady state detail for  $p_{up} = 820$  kPa. The black curves in (b) and (c) are experimental measurements, and the purple curves are the measured upstream pressure rise. The shaded regions represent the accuracy of the downstream pressure transducer. The accuracy of the pressure transducer is the main source of error at low pressures; at higher pressures, the sample-to-sample variation is the main source of error. The lower limit of detection of the downstream pressure detector is 0.1 Pa, resulting in steps in the measured downstream pressure. (d) Comparison of simulation with and without a dynamic increase in maximum absorbate concentration in the polymer. The experimental data for  $N_2$  permeation through sample L5S2 are in black. The upstream pressure rise is in purple. The correct simulation, with a dynamic increase in maximum concentration within the polymer, is shown in red. The simulation with all internal gas absorption sites available at the start of the upstream pressure rise is shown in blue. (For interpretation of the references to colour in this figure legend, the reader is referred to the web version of this article.)

the setup shown in Fig. 8, agrees with experiment (see SI Sect. 12 and Fig. S9) [52]. We apply this model to simulate permeation of mixtures containing several components of dry air:  $N_2$ ,  $O_2$ , Ar, and  $CO_2$ . All relevant input values for the simulations are reported in Table S4. In Fig. 11a, it is shown that the selectivity for  $CO_2$  in a mixture of gases, all at the same partial pressure, is near to its ideal selectivity ( $\approx 10\times$  that of  $N_2$  and  $\approx 5\times$  that of  $O_2$ ). However, the concentration of  $CO_2$  in air is low,  $p(CO_2) = 0.041$  kPa [53]. If the concentrations of gases are set to their concentrations in air (80 kPa for  $N_2$ , 21 kPa for  $O_2$ , and 0.95 kPa for Ar) [54], the permeation of  $CO_2$  nearly ceases, due to its extremely low partial pressure, as shown in Fig. 11b. The simulations enable a target permeability for  $CO_2$  to be estimated for a membrane that would selectively increase the  $CO_2$  concentration in air. Assuming a  $CO_2$  permeability value 100 times higher than for PDMS, with that for the other gases held constant, enrichment to 24% is predicted. This hypothetical situation is not achievable with a single component polymeric membrane because selectivity and permeability for gases of similar characteristics cannot be tuned independently [55]. To identify useful architectures, the model framework presented here can be extended to evaluate and compare new membrane design concepts prior to experimental study, such as layered and inorganic-organic

composites and supported ionic liquids. Information on performance characteristics of these systems under intermittent conditions can be obtained from the simulations [50].

## 6.2. Simulations of solar $CO_2$ reduction product crossover between electrode chambers during a diurnal cycle

Solar fuels generators [56] utilize membranes to separate the cathode and anode regions, and enable ion transfer between catholyte and anolyte during operation. For an example of the device architecture, see Ref. [57]. Reduced products are formed on the cathode side, and oxygen is formed on the anode side. The basic architecture of the commercial membranes used for solar hydrogen generators is a phase-separated polyelectrolyte with glassy regions that are impermeable to  $H_2$  and  $O_2$ , typically dissolved in electrolyte or present as gas bubbles, and hydrated channels with good ionic conductivity [58,59]. A recent modeling study has shown that the  $H_2$  and  $O_2$  product crossover-blocking property of a membrane for a photoelectrochemical hydrogen generation system is crucial for efficient operation, and can be achieved by reducing conductivity since the crossover path is typically through the hydrated ionic conduction channels [60].



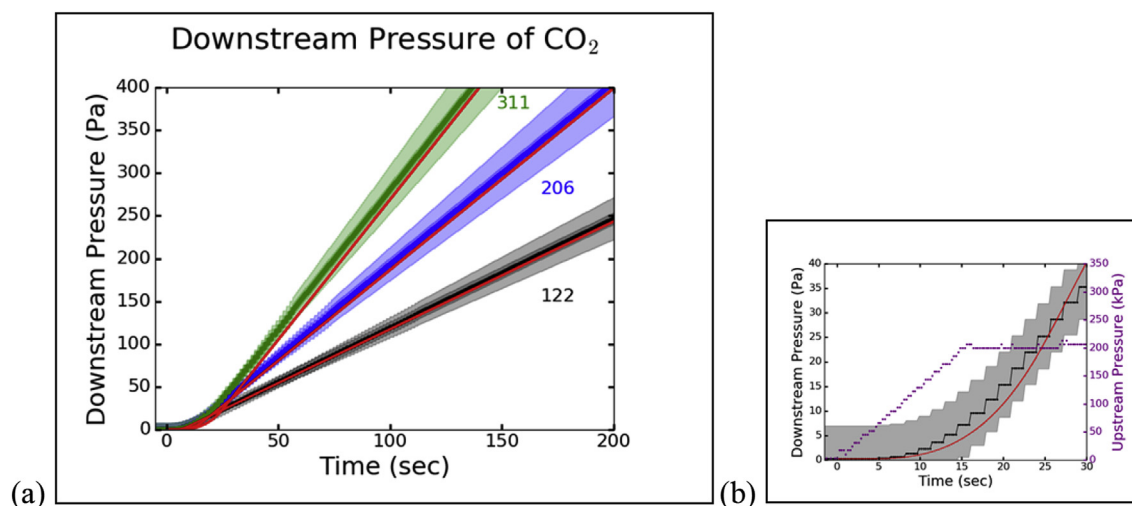


**Fig. 10.** Comparison of simulation and experiment permeation curves for CO<sub>2</sub>. The simulation results are shown in red. (a) Summary plot for all pressures. The shaded regions represent an experimental sample-to-sample standard deviation of 10%. Each curve is labeled with the upstream pressure in kPa. (b) Pre-steady state detail for  $p_{up} = 206$  kPa. The black curve is the experimental measurements, and the purple curve is the measured upstream pressure rise. The shaded region represents the accuracy of the downstream pressure transducer. The accuracy of the pressure transducer is the main source of error at low pressures; at higher pressures, the sample-to-sample variation is the main source of error. The lower limit of detection of the downstream pressure detector is 0.1 Pa, resulting in steps in the measured downstream pressure. (For interpretation of the references to colour in this figure legend, the reader is referred to the web version of this article.)

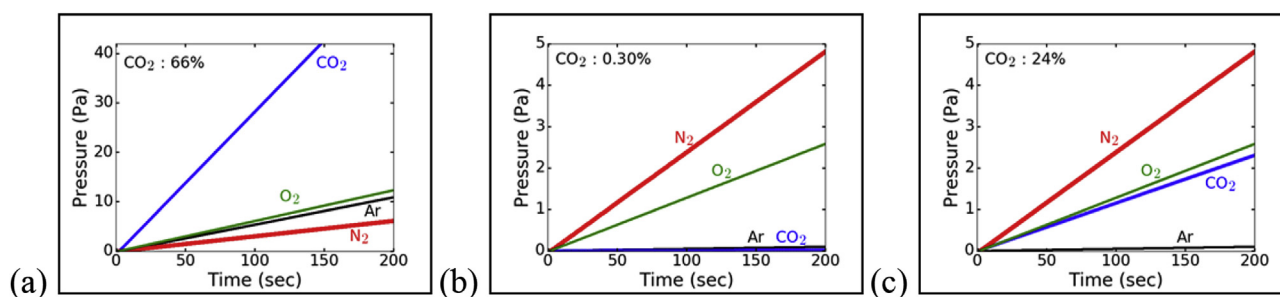


**Fig. 11.** Downstream gas composition for upstream mixtures of O<sub>2</sub>, N<sub>2</sub>, Ar and CO<sub>2</sub> as a function of time. (a) All four gases present at equal upstream partial pressure, resulting in a downstream mixture highly enriched in CO<sub>2</sub>. (b) Upstream gas mixture with the same composition as air permeating PDMS; minimal CO<sub>2</sub> permeation is observed due to its low upstream concentration. (c) Upstream gas mixture with the same composition as air permeating a hypothetical polymer with CO<sub>2</sub> permeability 100 times greater than PDMS, resulting in the downstream gas mixture containing 24% CO<sub>2</sub>.

Solar photoelectrochemical devices that convert CO<sub>2</sub> into reduced hydrocarbon and oxygenate products present a much more complicated situation. They usually generate mixtures on the cathode side, where each product may influence the others' transport processes through the membrane, and O<sub>2</sub> on the anode side, which can diffuse in the opposing direction. In a solar CO<sub>2</sub> reduction device (illustrated in Fig. 12a), the rate of product formation and the chemical composition of the products are voltage-dependent. The cell voltage is determined by the amount of sunlight incident on the light absorber in the device, varying with time of day, season, and weather [61]. It cannot be assumed that steady-state membrane operation is ever achieved; however multiphysics models generally do so because of the lack of information about their non-steady-state transport [62]. The glassy matrix blocks significant permeant crossover, but exposure of glassy polymers to CO<sub>2</sub> can cause them to plasticize, resulting in development of a rubbery character over time with increased permeability, and product crossover between the electrodes' chambers [55,60]. This will potentially reduce efficiency and selectivity of these systems. Modeling studies examining optimum membrane characteristics for CO<sub>2</sub> reduction systems have not been reported to our knowledge.

The model developed in the present work for PDMS permeated by CH<sub>4</sub>, a prototypical CO<sub>2</sub> reduction product, allows aspects of varying production rate and cross-over to be examined. Assumption of PDMS-like properties is a worst-case scenario, representing a membrane that has been extensively plasticized in use. The primary modification of the kinetic processes in the model is to change the simulated system from a gas-membrane system to an aqueous electrolyte-membrane system. Under such conditions, the interfacial interactions change, but transport within the membrane is unaltered if swelling and water uptake are negligible. The simulation setup for this case is shown in Fig. 12b. The surface adsorption rate constant  $k_{ads}$  (see Reaction 1) is calculated from the Smoluchowski equation for diffusion-controlled reactions, rather than as a scattering process as in the gas-polymer case. Using the diffusion coefficient of methane in water of  $2.35 \times 10^{-9}$  m<sup>2</sup>/s (at 308 K) [63] and an interaction distance of 4 Å, which is twice the van der Waals radius,  $k_{ads}$  is equal to  $7 \times 10^9$  M<sup>-1</sup> s<sup>-1</sup>. The diffusion coefficient of CH<sub>4</sub> molecules between electrolyte and interface compartments is set to 1 m<sup>2</sup>/s to represent a rapidly stirred electrolyte. It is assumed that once the permeant has traversed the membrane, it does not back-diffuse. It also assumed that the catholyte is well mixed but not recirculated, allowing products to

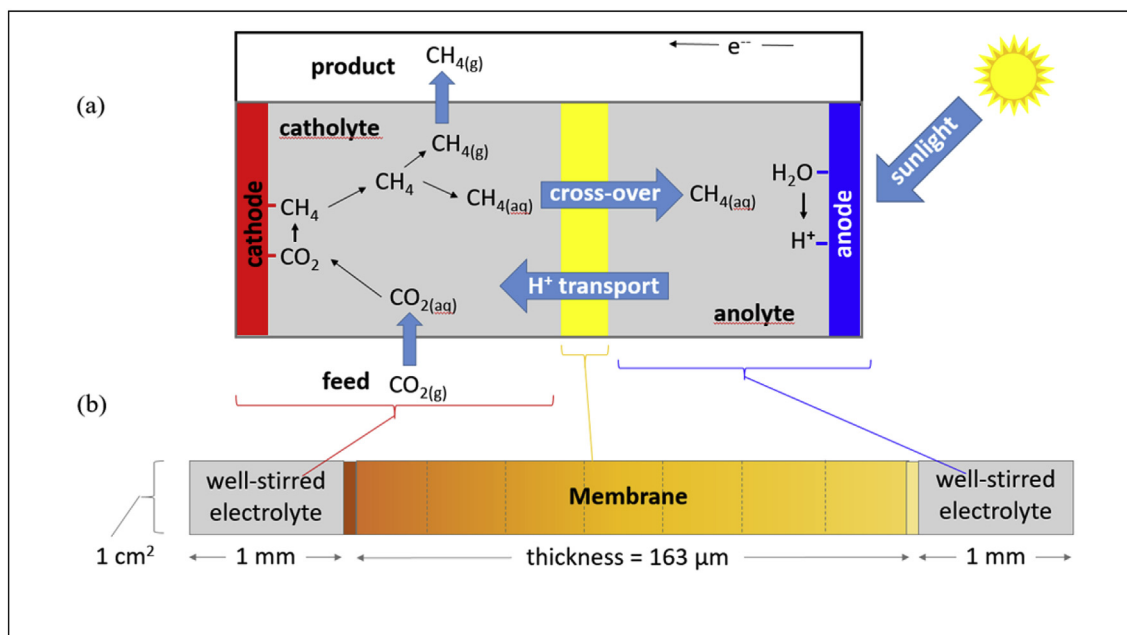
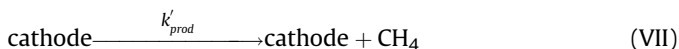


**Fig. 12.** Overview of a solar fuels device and its multi-scale model. (a) An example of a solar fuels device with a face-to-face architecture, in which the cathode, anode, and membrane all have the same area, and the membrane is separated from the catalyst layers by aqueous electrolyte. The reduction of  $\text{CO}_2$  to  $\text{CH}_4$  is shown, including electron transport, proton transport, carbon dioxide transport, carbon dioxide reduction reaction, and methane desorption, along with the possibilities for  $\text{CH}_4$  to become hydrated and cross over the membrane or to enter gas phase and be collected in the product stream. Protons for the reduction reaction are generated at the anode via a water-splitting reaction. Details of the proton transport depend upon the pH, the buffer system, and the membrane type, and are omitted here. (b) In the multi-scale model, the catalysts are combined with their electrolyte regions to form a single well-stirred electrolyte compartment. The catholyte compartment contains a simplified version of all the chemistry occurring at the cathode surface, representing all the reactive steps and the desorption step by a single step for methane production. No chemistry occurs in the simulated anode region, which serves simply as a collection compartment for  $\text{CH}_4$  in this work. The geometry is that of a typical solar fuels device prototype with 1 cm [2] cross-sectional area and 1 mm thick electrolyte compartments. The interfacial regions between electrolyte and membrane are 1 nm thick.

accumulate.

If only  $\text{CH}_4$  is produced at a typical current density for a solar photoelectrochemical device of  $0.010 \text{ A/cm}^2$ , a production rate of  $13 \times 10^{-9} \text{ mol/(cm}^2 \text{ s)}$  is expected assuming the catalyst area is equal to the geometric area of the cathode [64]. For the combined cathode-catholyte region used in the simulations, the  $\text{CH}_4$  production rate per area converts to a volumetric production rate of  $\chi_{\text{prod}} = 1.30 \times 10^{-4} \text{ mol/(L s)}$ . Because photocurrent scales with time of day, the rate of  $\text{CH}_4$  production would be at its maximum only when insolation is at its maximum [61]. For simplicity, this diurnal variation is described as a simple triangle wave lasting a total of 8 h, shown in Fig. 13a. An extended period of darkness follows during which no additional  $\text{CH}_4$  is produced but that which remains dissolved in the electrolyte can permeate the membrane. The  $\text{CH}_4$  production reaction step is implemented as a pseudo-0<sup>th</sup> order reaction



where  $k'_{\text{prod}} = r_{\text{sun}} \times \chi_{\text{prod}}$ , and  $r_{\text{sun}}$  is the ratio of current sunlight level to the maximum amount of sunlight. This representation is used because it allows a correct generation rate without specifying detailed surface kinetics. Once formed, methane may dissolve up to its solubility limit in water of 0.001 M (for 308 K) [65], represented as an aqueous solution site, “aq-site,”



or bubble out of solution as a gas



where the zeroth order rate constants (now equal to the rates) for hydration,  $k_{\text{hyd}} = 10^{50} \text{ mol/(L s)}$ , and bubbling out,  $k_{\text{bub}} = 10^{25} \text{ mol/(L s)}$ , are arbitrarily high to represent nearly instantaneous processes. The larger rate constant for hydration ensures that the methane molecules remain in water if an aqueous site is available; if no site is available, the methane molecule will bubble out of solution instead. It is assumed that the electrolyte is rapidly stirred such that boundary layer and mass transport limitations are negligible.

The transport properties of  $\text{CH}_4$  in PDMS and two hypothetical polymers (Hyp1 and Hyp2) are listed in Table 4. Both hypothetical polymers have a permeability three orders of magnitude lower than PDMS. For Hyp1, all reduction in permeability comes from a reduction in the diffusivity; for Hyp2, all reduction in permeability comes from a reduction in the solubility. As a point of reference, the values of  $D$  and  $S$  for Hyp1 are similar to those for polystyrene [66].

The amount of  $\text{CH}_4$  produced from Reaction VII over time is shown in Fig. 13b and is the same for all three simulations. The rate of  $\text{CH}_4$  production increases over the first 4 h, reaches its maximum at the peak of available sunlight, then declines over the next 4 h, resulting in a total production of  $1.87 \times 10^{-4} \text{ mol}$  of  $\text{CH}_4$ . Because the solubility limit for gases in water is low, a constant aqueous concentration of  $\text{CH}_4$  is rapidly established, as shown for PDMS, Hyp1, and Hyp2 in Fig. 14a, d, and 14g, respectively. Additional  $\text{CH}_4$  produced bubbles out as a gaseous product, as shown for PDMS, Hyp1, and Hyp2 in Fig. 14b, e, and 14h, respectively. For a theoretical, completely blocking membrane, the maximum aqueous concentration is reached in 7.8 min. Hyp1 and Hyp2 come close to

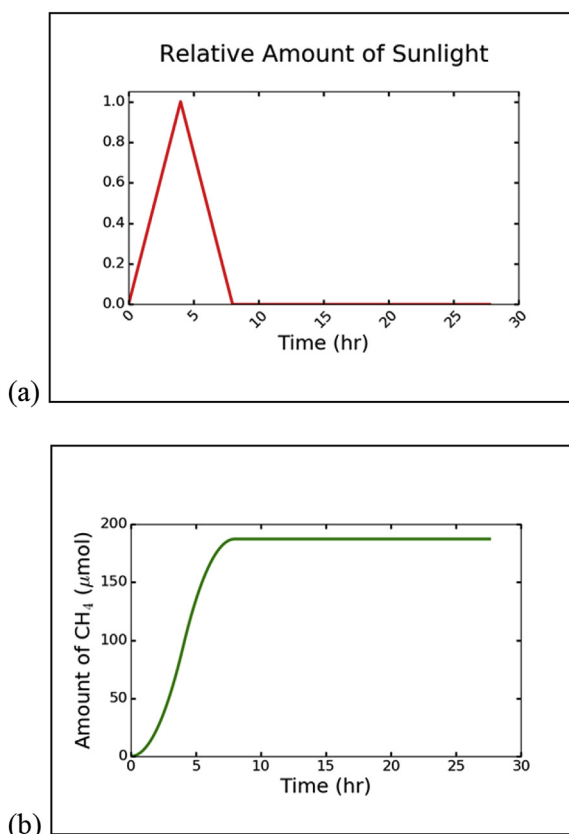


**Fig. 13.** The production of CH<sub>4</sub>. (a) The normalized level of sunlight, which is a multiplier for the rate constant for CH<sub>4</sub> production. (b) The total amount of CH<sub>4</sub> produced from Reaction VII, including both those that will become gaseous and those that will become hydrated.

**Table 4**

Properties of the membranes used in the diurnal cycle simulations.

Polymer	$S$ (mol/L)/(mol/L) <sup>a</sup>	$D$ m <sup>2</sup> /s	$P_m$ m <sup>2</sup> /s
PDMS <sup>b</sup>	0.467	$2.20 \times 10^{-9}$	$1.03 \times 10^{-9}$
Hyp1	0.467	$2.20 \times 10^{-12}$	$1.03 \times 10^{-12}$
Hyp2	$4.67 \times 10^{-4}$	$2.20 \times 10^{-9}$	$1.03 \times 10^{-12}$

<sup>a</sup> The units for solubility are mol/L inside of the polymer per mol/L in the external electrolyte.

<sup>b</sup> Reference [40].

this, with aqueous phase saturation occurring within 10 min, at which time, sunlight is less than 10% of its maximum level. The concentration profiles of CH<sub>4</sub> within all three membranes are available in the SI Section 13, Fig. S10. The concentration profile of CH<sub>4</sub> within the hypothetical membranes also reaches steady state within 10 min. In PDMS, these processes take 20 min. The delay in reaching steady state, compared to the hypothetical membranes, is due to the high permeability of PDMS. As CH<sub>4</sub> is entering the aqueous phase near the cathode, it is also being removed by transport across the membrane, thus delaying the build-up to its maximum concentration. However, this build-up is only a small fraction of the device's operating time.

Once CH<sub>4</sub> production ceases, it takes only about 1 min for the remaining CH<sub>4</sub> to traverse the PDMS membrane into the anode chamber. This means that for a very permeable membrane, any CH<sub>4</sub> present in the aqueous phase will cross over the membrane. In contrast, the depletion of CH<sub>4</sub> from the catholyte and emptying of

the remaining CH<sub>4</sub> within the membrane is estimated to take over 40 h for the less permeable membranes. In this case, the enhanced blocking capabilities of these membranes are due not only to lower steady-state permeability but also retention of product within the membrane during dark hours, as can be seen in the concentration profiles in the SI Section 13, Fig. S10. The membrane is a key contributor to the ability to recover products from solar fuels devices. The maximum possible amount of product that can be recovered is equal to the total amount of gas produced, shown for PDMS, Hyp1, and Hyp2 in Fig. 14b, e, and 14h, respectively. Conversely, the total amount of methane cross-over for PDMS, Hyp1, and Hyp2 are shown in Fig. 14c, f, and 14i, respectively. For PDMS,  $\approx 10\%$  of CH<sub>4</sub> crosses the membrane. Because CH<sub>4</sub> is highly permeable in PDMS, 25% represents an approximate upper bound on gaseous product loss, though products with higher solubility in water may experience even greater losses. By reducing the permeability by three orders of magnitude, recovery can be increased to 99.96%. It does not matter whether this decrease in permeability results from changes in diffusivity or solubility. Even with low permeability, however, it is unlikely that product cross-over can be prevented completely.

This is an interesting situation because the solar-fuels device is operating under continually changing conditions, so the rate of methane production is changing continually as well. However, the aqueous concentration of methane is constant over most of the operating time, and the membrane is essentially experiencing steady-state conditions with respect to this permeant during daylight hours. Using a more realistic insolation profile or including the fluctuations in sunlight that are present under real-world operating conditions will have little effect on the operation of the membrane, at least for the conditions studied herein. Fluctuations in sunlight levels may play a greater role in other types of systems, for example, when the production rate is lower, the aqueous solubility is higher, or the permeability is higher.

## 7. Summary and conclusions

In this work we describe a multiscale modeling study of permeation of rubbery polymer membranes by simple inert solutes, with the goal of developing a full description of steady-state and non-steady-state processes. We have chosen to focus on these systems as a simplest case since the polymer transport properties, solubility and diffusivity, are expected to be constant over time. We have confirmed that the permeation process is insensitive to permeant adsorption and absorption kinetics in these systems, consistent with the assumption made in the solution-diffusion model for membrane permeation. Two quantitatively validated models, built on a common reaction-diffusion framework, are reported: quenching of PtOEP phosphorescent dye in C4PTP, an oxygen sensor system, and permeation of O<sub>2</sub>, N<sub>2</sub>, CH<sub>4</sub> and CO<sub>2</sub> through a PDMS separator. The predictive framework is extended to simulate two additional hypothetical systems, separation of CO<sub>2</sub> from air using a PDMS-like membrane, and crossover of the CO<sub>2</sub> reduction product, CH<sub>4</sub>, in a solar-fuels system whose membrane separator is rubbery or glassy, but inert to the permeant.

Because the goal is the development of a quantitatively predictive model with no adjustable parameters, the model construction process is dependent on time-dependent permeation data as well as experimental and theoretical information on specific materials properties and processes. Such data are not commonly available in the literature so experimental and MD computational studies have been performed and are reported in this paper. The results show that a simple reaction-diffusion framework simulated using stochastic methods is adequate to capture the details of interfacial processes as well as bulk processes, covering a broad

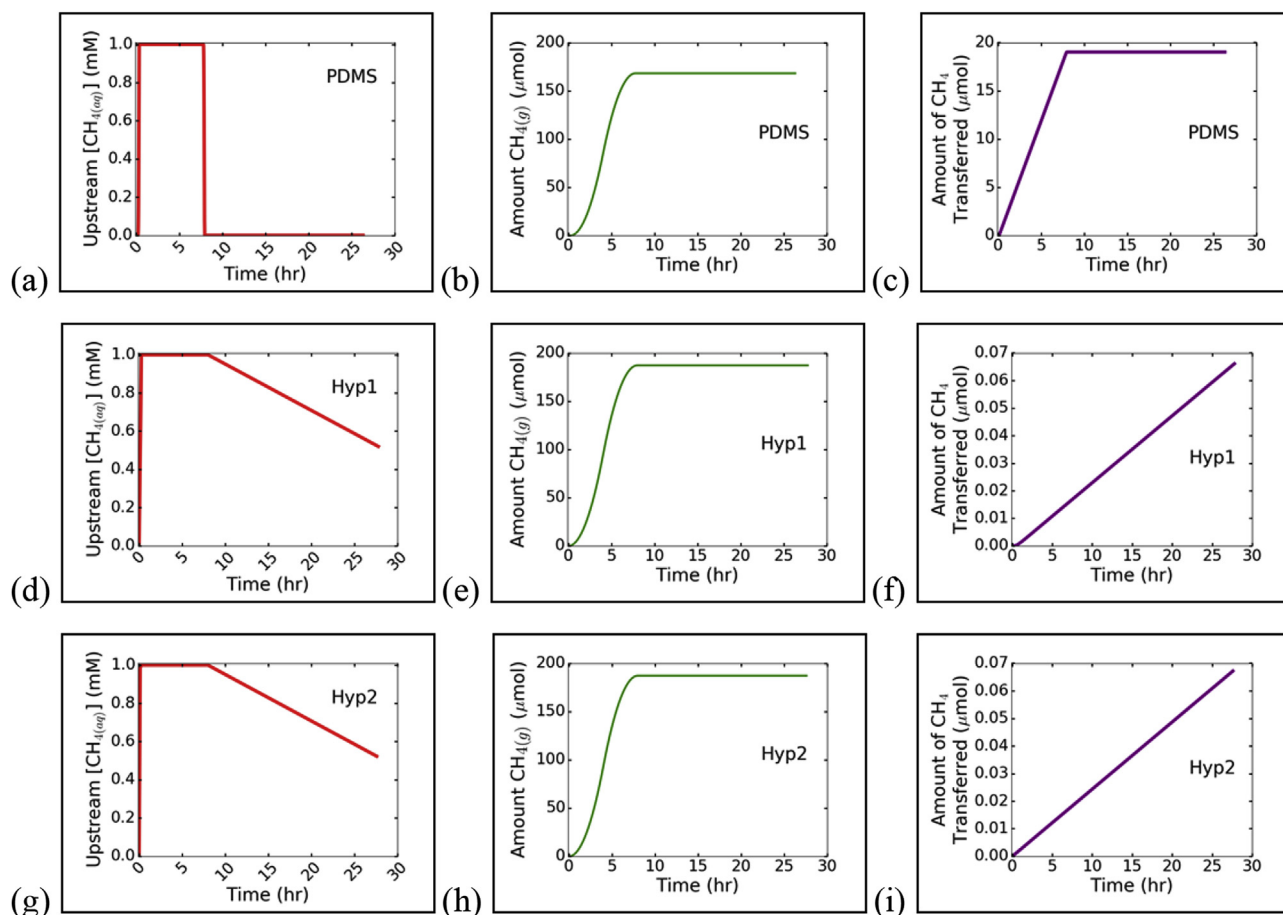


**Fig. 14.** Results of membrane crossover simulations during diurnal photoelectrochemical CH<sub>4</sub> production. (a)–(c) PDMS, (d)–(f) Hyp1, (g)–(i) Hyp2. (a), (d), (g) Upstream concentration of dissolved CH<sub>4</sub> in the cathode chamber stays at the aqueous solubility limit during insolation. The remaining CH<sub>4</sub> is rapidly depleted by crossing the PDMS membrane but is slowly depleted for the two hypothetical membranes due to their low permeability. (b), (e), (h) Amount of CH<sub>4</sub> that enters the gas phase and can be collected as a product. (c), (f), (i) Amount of CH<sub>4</sub> that crosses over the membrane and so is not collected as product. The results for the two hypothetical membranes are nearly identical due to their identical permeabilities.

range of length- and timescales. Measured quantities such as solubilities and diffusion coefficients contain enough information about solute-polymer interactions to predict experimental observables such as pressure increases and phosphorescence quenching as investigated here without explicit inclusion of free volume dynamics and tortuosity, although these elements can be built into the model with straightforward modifications.

Several new insights to polymer-permeant systems have been obtained through the simulations.

- (i) Time-dependent phosphorescence quenching is related in a complicated way to the amount of O<sub>2</sub> sorbed into a polymer due to the rate mismatch between dye-O<sub>2</sub> interactions and O<sub>2</sub> transport. This suggests that such sensors are best used in conjunction with models such as that presented here to ensure complete data interpretation.
- (ii) The pre-steady state portion of a gas permeation curve contains a great deal of information about the nature of the gas-polymer interaction. In particular, we find it necessary to include a dynamically increasing maximum concentration within the polymer as the upstream permeant pressure increases, in accordance with Henry's law solubility, to reproduce the experimental data successfully. This raises interesting questions about what is occurring inside the polymer during a pressure rise, especially how interfacial

processes affect the polymer bulk, and how fast this response is.

- (iii) During intermittent operation such as a diurnal cycle, low-permeability membranes can continue to permit crossover long after product formation has ceased due to slow permeation of residual products in the electrolyte. This effect needs to be taken into account for successful membrane and separation systems design for complex situations such as solar fuels generators and CO<sub>2</sub> capture.

## Conflicts of interest

None.

## Acknowledgements

This material is based upon work performed by the Joint Center for Artificial Photosynthesis, a DOE Energy Innovation Hub, as follows: The reaction-diffusion simulations were performed by M. S. and F. H., and experimental measurements were performed by M. T. and A. W., supported through the Office of Science of the U.S. Department of Energy under Award Number DE-SC0004993. M. T. thanks the National Science Foundation Graduate Research Fellowship under Grant No. DGE 1106400. D. B., B. M. and W. A. G.



acknowledge funding from Bosch Energy Research Network Grant No 07.23.CS.15 for the MD simulation work. Bosch Energy Research had no involvement in decisions concerning data collection, data processing, writing, or article submission. The authors are grateful to Dr. Daniel J. Miller (JCAP, LBNL) for many helpful discussions on membrane polymer science, to Mr. Ezra L. Clark (JCAP, LBNL) for data on photoelectrochemical production of methane, and to Dr. William D. Hinsberg (Columbia Hill Technical Consulting) for discussions on the use of Kinetiscope in this work.

## Appendix A. Supplementary data

Supplementary data related to this article can be found at: <https://doi.org/10.1016/j.polymer.2017.11.055>. Tables containing the data used to prepare the figures in this article and additional experimental data are located at <https://doi.org/10.18734/P4Z071>.

## References

- [1] M. Mulder, Basic Principles of Membrane Technology, Kluwer Academic Publishers, Dordrecht, The Netherlands, 1996.
- [2] J.G. Wijmans, R.W. Baker, The solution-diffusion model - a review, *J. Membr. Sci.* 107 (1–2) (1995) 1–21.
- [3] J. Crank, G.S. Park, Diffusion in Polymers, Academic Press Inc., Ltd., London and New York, 1968.
- [4] D.W. Shin, M.D. Guiver, Y.M. Lee, Hydrocarbon-based polymer electrolyte membranes: importance of morphology on ion transport and membrane stability, *Chem. Rev.* 117 (6) (2017) 4759–4805.
- [5] A. Kusoglu, A.Z. Weber, Study of PFSA ionomers using X-ray scattering techniques, *Abstr. Pap. Am. Chem. S* 248 (2014).
- [6] C.N. Jayarajah, Luminescence Quenching Studies of Oxygen Diffusion in Highly Permeable Media, University of Toronto, 1998.
- [7] C.N. Jayarajah, A. Yekta, I. Manners, M.A. Winnik, Oxygen diffusion and permeability in alkylaminophenylphosphazene films intended for phosphorescence barometry applications, *Macromolecules* 33 (15) (2000) 5693–5701.
- [8] X.-d. Wang, O.S. Wolfbeis, Optical methods for sensing and imaging oxygen: materials, spectroscopies and applications, *Chem. Soc. Rev.* 43 (2014) 3666–3761.
- [9] D. Bunker, B. Garrett, T.G.L. Kleindienst III, Discrete simulation methods in combustion kinetics, *Combust. Flame* 23 (1974) 373–379.
- [10] D.T. Gillespie, General method for numerically simulating stochastic time evolution of coupled chemical-reactions, *J. Comput. Phys.* 22 (4) (1976) 403–434.
- [11] W.D. Hinsberg, F.A. Houle, Kinetiscope, [www.hinsberg.net/kinetiscope](http://www.hinsberg.net/kinetiscope), 2015.
- [12] F.A. Houle, W.D. Hinsberg, M. Morrison, M.I. Sanchez, G. Wallraff, C. Larson, J. Hoffnagle, Determination of coupled acid catalysis-diffusion processes in a positive-tone chemically amplified photoresist, *J. Vac. Sci. Technol. B Microelectron. Nanom. Struct.* 18 (2000) 1874.
- [13] F.A. Houle, W.D. Hinsberg, M.I. Sanchez, Kinetic model for positive tone resist dissolution and roughening, *Macromolecules* 35 (2002) 8591–8600.
- [14] A.A. Wiegel, K.R. Wilson, W.D. Hinsberg, F.A. Houle, Stochastic methods for aerosol chemistry: a compact molecular description of functionalization and fragmentation in the heterogeneous oxidation of squalene aerosol by OH radicals, *Phys. Chem. Chem. Phys.* 17 (2015) 4398–4411.
- [15] A.A. Wiegel, M. Liu, W.D. Hinsberg, K.R. Wilson, F.A. Houle, Diffusive confinement of free radical intermediates in the OH radical oxidation of semisolid aerosol, *Phys. Chem. Chem. Phys.* 19 (2017) 6814–6830.
- [16] G. Wallraff, J. Hutchinson, W. Hinsberg, F. Houle, P. Seidel, R. Johnson, W. Oldham, Thermal and acid-catalyzed deprotection kinetics in candidate deep ultraviolet resist materials, *J. Vac. Sci. Technol. B Microelectron. Nanom. Struct.* 12 (6) (1994), 3857–3857.
- [17] F.A. Houle, W.D. Hinsberg, M.I. Sanchez, J.A. Hoffnagle, Influence of resist components on image blur in a patterned positive-tone chemically amplified photoresist, *J. Vac. Sci. Technol. B Microelectron. Nanom. Struct.* 20 (3) (2002), 924–924.
- [18] K. Bowers, E. Chow, H. Xu, R. Dror, M. Eastwood, B. Gregersen, J. Klepeis, I. Kolossvary, M. Moraes, F. Sacerdoti, J. Salmon, Y. Shan, D. Shaw, Scalable algorithms for molecular dynamics simulations on commodity clusters, *ACM/IEEE S. C. 2006 Conf. (SC'06)* (2006) (November), 43–43.
- [19] D. Shivakumar, J. Williams, Y. Wu, W. Damm, J. Shelley, W. Sherman, Prediction of absolute solvation free energies using molecular dynamics free energy perturbation and the OPLS force field, *J. Chem. Theory Comput.* 6 (2010) 1509–1519.
- [20] Z. Guo, U. Mohanty, J. Noehre, T.K. Sawyer, W. Sherman, G. Krilov, Probing the  $\alpha$ -helical structural stability of coupled p53 peptides: molecular dynamics simulations and analysis, *Chem. Biol. Drug Des.* 75 (2010) 348–359.
- [21] J.L. Banks, H.S. Beard, Y. Cao, A.E. Cho, W. Damm, R. Farid, A.K. Felts, T.A. Halgren, D.T. Mainz, J.R. Maple, R. Murphy, D.M. Philipp, M.P. Repasky, L.Y. Zhang, B.J. Berne, R.A. Friesner, E. Gallicchio, R.M. Levy, Integrated modeling program, applied chemical theory (IMPACT), *J. Comput. Chem.* 26 (16) (2005) 1752–1780.
- [22] D.A. McQuarrie, Statistical Mechanics, University Science Books, Mill Valley, CA, 2000 p 641.
- [23] G.J. Martyna, D.J. Tobias, M.L. Klein, Constant pressure molecular dynamics algorithms, *J. Chem. Phys.* 101 (5) (1994), 4177–4177.
- [24] H. Shin, T.A. Pascal, W.A. Goddard, H. Kim, Scaled effective solvent method for predicting the equilibrium ensemble of structures with analysis of thermodynamic properties of amorphous polyethylene glycol-water mixtures, *J. Phys. Chem. B* 117 (3) (2013) 916–927.
- [25] Polymer Data Handbook, Oxford University Press, 1999 p 1012.
- [26] A.P. Willard, D. Chandler, Instantaneous liquid interfaces, *J. Phys. Chem. B* 114 (5) (2010) 1954–1958.
- [27] J. Julin, M. Shiraiwa, R.E.H. Miles, J.P. Reid, U. Pöschl, I. Riipinen, Mass accommodation of water: bridging the gap between molecular dynamics simulations and kinetic condensation models, *J. Phys. Chem. A* 117 (2) (2013) 410–420.
- [28] J. Julin, P.M. Winkler, N.M. Donahue, P.E. Wagner, I. Riipinen, Near-unity mass accommodation coefficient of organic molecules of varying structure, *Environ. Sci. Technol.* 48 (2014) 12083–12089.
- [29] Springer Handbook of Materials Measurement Methods, Springer, Berlin, 2006, p. 1207.
- [30] Model super TJE: ultra precision pressure transducer, HoneyWell, <https://measurementsensors.honeywell.com/Pages/Product.aspx?category=&cat=Honeywell&pid=stje>. (Accessed 24 March 2017).
- [31] "Baratron General Purpose Capacitance Manometers: 750C11T," MKS Instruments. <https://www.mksinst.com/product/product.aspx?ProductID=126> (accessed March 24, 2017).
- [32] K. Hodge, T. Prodpran, N.B. Shenogina, S. Nazarenko, Diffusion of oxygen and carbon dioxide in thermally crystallized syndiotactic polystyrene, *J. Polym. Sci. Part B Polym. Phys.* 39 (2001) 2519–2538.
- [33] A.K. Bansal, W. Holzer, A. Penzkofer, T. Tsuboi, Absorption and emission spectroscopic characterization of platinum-octaethyl-porphyrin (PtOEP), *Chem. Phys.* 330 (1–2) (2006) 118–129.
- [34] T. Engel, P. Reid, Thermodynamics, Statistical Thermodynamics, & Kinetics, second ed., Prentice Hall, 2010, p. p 602.
- [35] G.A. Somorjai, Y. Li, Introduction to Surface Chemistry and Catalysis, Wiley, 2010, p. p 800.
- [36] P. Atkins, J. de Paula, Physical Chemistry, eighth ed., W. H. Freeman and Co., New York, USA, 2006, p. p 1053.
- [37] P. Houston, Chemical Kinetics and Reaction Dynamics, Dover Publications, Inc., Mineola, New York, 2001, p. p 518.
- [38] T. Dienel, H. Proehl, T. Fritz, K. Leo, Novel near-infrared photoluminescence from platinum(II)-porphyrin (PtOEP) aggregates, *J. Luminescence* 110 (2004) 253–257.
- [39] A. Yekta, Z. Masoumi, M.A. Winnik, Luminescence measurements of oxygen permeation and oxygen diffusion in thin polymer films, *Can. J. Chem.* 73 (11) (1995) 2021–2029.
- [40] T.C. Merkel, V.I. Bondar, K. Nagai, B.D. Freeman, I. Pinnau, Gas sorption, diffusion, and permeation in poly(dimethylsiloxane), *J. Polym. Sci. Part B Polym. Phys.* 38 (3) (2000) 415–434.
- [41] L. Brandão, L.M. Madeira, A.M. Mendes, Mass transport on composite dense PDMS membranes with palladium nanoclusters, *J. Membr. Sci.* 288 (1–2) (2007) 112–122.
- [42] K. Berean, J.Z. Ou, M. Nour, K. Latham, C. McSweeney, D. Paull, A. Halim, S. Kentish, C.M. Doherty, A.J. Hill, K. Kalantar-zadeh, The effect of crosslinking temperature on the permeability of PDMS membranes: evidence of extraordinary CO<sub>2</sub> and CH<sub>4</sub> gas permeation, *Sep. Purif. Technol.* 122 (2014) 96–104.
- [43] D.K. Lancaster, A.M. Johnson, D.K. Burden, J.P. Wiens, G.M. Nathanson, Inert gas scattering from liquid hydrocarbon microjets, *J. Phys. Chem. Lett.* 4 (18) (2013) 3045–3049.
- [44] J.W. Lu, J.R. Morris, Gas-Surface scattering dynamics of CO<sub>2</sub>, NO<sub>2</sub>, and O<sub>3</sub> in collisions with model organic surfaces, *J. Phys. Chem. A* 115 (2011) 6194–6201.
- [45] W.A. Alexander, J. Zhang, V.J. Murray, G.M. Nathanson, T.K. Minton, Kinematics and dynamics of atomic-beam scattering on liquid and self-assembled monolayer surfaces, *Faraday Discuss.* 157 (2012) 355–374.
- [46] D.J. Donaldson, Adsorption of atmospheric gases at the Air–Water interface. I. NH<sub>3</sub>, *J. Phys. Chem. A* 103 (1) (1999) 62–70.
- [47] H. Ogasawara, N. Horimoto, M. Kawai, Ammonia adsorption by hydrogen bond on ice and its solvation, *J. Chem. Phys.* 112 (19) (2000) 8229–8232.
- [48] Y.P. Yampolskii, I. Pinnau, B.D. Freeman, Materials Science of Membranes for Gas and Vapor Separation, John Wiley & Sons Ltd, West Sussex, England, 2006, 445–445.
- [49] K.Z. House, A.C. Baclig, M. Ranjan, E.A. van Nierop, J. Wilcox, H.J. Herzog, Economic and energetic analysis of capturing CO<sub>2</sub> from ambient air, *Proc. Natl. Acad. Sci.* 108 (51) (2011) 20428–20433.
- [50] C.W. Jones, CO<sub>2</sub> capture from dilute gases as a component of modern global carbon management, *Annu. Rev. Chem. Biomol. Eng.* 2 (2011) 31–52.
- [51] S.S. Dhingra, E. Marand, Mixed gas transport study through polymeric membranes, *J. Membr. Sci.* 141 (1998) 45–63.
- [52] F. Wu, L. Li, Z. Xu, S. Tan, Z. Zhang, Transport study of pure and mixed gases through PDMS membrane, *Chem. Eng. J.* 117 (2006) 51–59.
- [53] "Recent Global CO<sub>2</sub>," Earth System Research Laboratory Global Monitoring Division. <https://www.esrl.noaa.gov/gmd/ccgg/trends/global.html> (accessed

- June 16, 2017).
- [54] IUPAC, Compendium of Chemical Terminology, second ed., vol. 2017, Blackwell Scientific Publications, Oxford, 1997.
- [55] D.F. Sanders, Z.P. Smith, R. Guo, L.M. Robeson, J.E. McGrath, D.R. Paul, B.D. Freeman, Energy-efficient polymeric gas separation membranes for a sustainable future: a review, *Polymer* 54 (18) (2013) 4729–4761.
- [56] C. Xiang, A.Z. Weber, S. Ardo, A. Berger, Y.K. Chen, R. Coridan, K.T. Fountaine, S. Haussener, S. Hu, R. Liu, N.S. Lewis, M.A. Modestino, M.M. Shaner, M.R. Singh, J.C. Stevens, K. Sun, K. Walczak, Modeling, simulation, and implementation of solar-driven water-splitting devices, *Angew. Chem. - Int. Ed.* 55 (42) (2016) 12974–12988.
- [57] M.R. Singh, E.L. Clark, A.T. Bell, Effects of electrolyte, catalyst, and membrane composition and operating conditions on the performance of solar-driven electrochemical reduction of carbon dioxide, *Phys. Chem. Chem. Phys.* 17 (29) (2015) 18924–18936.
- [58] F.I. Allen, L.R. Comolli, A. Kusoglu, M.A. Modestino, A.M. Minor, A.Z. Weber, Morphology of hydrated as-cast Nafion revealed through cryo electron tomography, *ACS Macro Lett.* 4 (1) (2015) 1–5.
- [59] A. Kusoglu, A.Z. Weber, New insights into perfluorinated sulfonic-acid ionomers, *Chem. Rev.* 117 (2016) 987–1104.
- [60] A. Berger, R.A. Segalman, J. Newman, Material requirements for membrane separators in a water-splitting photoelectrochemical cell, *Energy & Environ. Sci.* 7 (4) (2014) 1468–1476.
- [61] Y. Chen, N.S. Lewis, C. Xiang, Modeling and simulation of the spatial and light-intensity dependence of product distributions in an integrated photoelectrochemical CO<sub>2</sub> reduction system, *ACS Energy Lett.* 1 (1) (2016) 273–280.
- [62] J.C. Stevens, A.Z. Weber, A computational study of optically concentrating, solar-fuels generators from annual thermal and fuel-production efficiency perspectives, *J. Electrochem. Soc.* 163 (7) (2016) H475–H484.
- [63] B. Jähne, G. Heinz, W. Dietrich, Measurement of the diffusion coefficients of sparingly soluble gases in water, *J. Geophys. Res. Oceans* 92 (C10) (1987) 10767–10776.
- [64] E.L. Clark, Personal Communication, 2016.
- [65] H.L. Clever, C.L. Young, "Methane". IUPAC Solubility Data Series, 27/28, Pergamon Press, Oxford, England, 1987.
- [66] D.H. Rein, R.F. Baddour, R.E. Cohen, Gas solubility and diffusion in a polystyrene-polybutadiene block copolymer, *J. Appl. Polym. Sci.* 45 (7) (1992) 1223–1227.